Plasma Sources Sci. Technol. **8** (1999) R45–R64. Printed in the UK PII: S0963-0252(99)03745-7

REVIEW ARTICLE

Ion energy distributions in rf sheaths; review, analysis and simulation

E Kawamura†, V Vahedi‡, M A Lieberman† and C K Birdsall†

† EECS Department, 195M Cory Hall, University of California at Berkeley, Berkeley, CA 94720-1770, USA
‡ Lam Research Corporation, 4650 Cushing Parkway, Fremont, CA 94538-6470, USA

Received 2 November 1998, in final form 13 April 1999

Abstract. We present a review and analysis of ion energy distributions (IED) arriving at the target of a radio frequency (rf) discharge. We mainly discuss the collisionless regime, which is of great interest to experimentalists and modellers studying high-density discharges in which the sheath is much thinner than in conventional reactive ion etching systems. We assess what has been done so far and determine what factors influence the shape of the IEDs. We also briefly discuss collisional effects on the IEDs. Having determined the important parameters, we perform some particle-in-cell simulations of a collisionless current-driven rf sheath which show that ion modulations in an rf sheath significantly affect the IEDs when $\tau_{ion}/\tau_{rf} < 1$, where τ_{ion} is the ion transit time and τ_{rf} is the rf period.

1. Introduction

In processing plasmas, the ion energy and angular distributions (IEDs and IADs) arriving at the wafer target are crucial in determining ion anisotropy and etch rates. High-density plasma sources are widely studied and characterized due to their growing use in semiconductor manufacturing and fabrication [1–4]. These plasma sources are typically operated at higher densities and lower pressures in order to obtain higher etch rates and better ion anisotropy at the target. Furthermore, most high-density sources operate with reduced sheath voltage drops in order to reduce ion bombarding damage and achieve ion energy control. In this regime, the ion motion in the radio frequency (rf) sheath is essentially collisionless since the sheath width is much smaller than the ion mean free path. Ion energy and angular spreads due to collisions within the sheaths are minimal.

In contrast, due to high operating pressures (approximately a few hundred mTorr) and large sheath voltage drops (∼1000 V), the sheaths in conventional reactive ion etching (RIE) sources are typically collisional. Most of the ion energy spread is caused by ion–neutral collisions, and the IED was shown to have multiple peaks and a large spread [5–8].

Because of the complexity of rf sheath dynamics, most calculations of IEDs rely on numerical methods. Closed form analytical expressions for IEDs in rf plasma reactors are rare and obtainable only after making very limiting approximations. IEDs have been calculated by approximate analytical models [9–11], the numerical integration of the equations of motion [5, 6, 8, 12–14], Monte Carlo simulations [7, 15–18] and particle-in-cell (PIC) methods [19, 20].

The energies of the bombarding ions have been measured by electrostatic deflection analysers [3, 21–27], cylindrical mirror analysers [28–34] or retarding grid analysers [4, 5–7, 35]. In some cases, quadrupole mass spectrometers were used to make mass resolved measurements, making it possible to compare the IEDs of different ionic species in the same discharge.

In this paper, we review and discuss IEDs within an rf sheath. In a collisionless dc discharge, we expect the IEDs to be monoenergetic about $e\bar{V}_s$, where $\bar{V}_s$ is the dc sheath voltage drop. However, in rf discharges, ion modulation can cause large ion energy spreads, which can also give rise to angular spreads. First, we examine some analytical models of the collisionless rf sheath in both the *high-* and *low-*frequency regimes. These regimes will be described below. For the low-frequency regime, we introduce an analytical model for an rf sheath. This model compares well with the more accurate numerical model of Metze *et al* [36] (1986), and it provides analytical solutions for the voltage and current waveforms in a low-frequency rf sheath. The model is also used to simplify the calculations made by Song *et al* [37] (1990) in deriving the bias voltage between electrodes in an asymmetric discharge. Second, we look at some more complicated numerical models of the collisionless rf sheath. Third, we briefly discuss the effect of collisions on IEDs and IADs. Fourth, we describe some of the experimental results on IEDs in rf sheaths. Finally, we discuss the results of PIC simulations of an rf sheath.

2. Theory of the collisionless rf sheath

2.1. High- and low-frequency regimes

In collisionless sheaths, the crucial parameter determining the shape of the IEDs is $\tau_{ion}/\tau_{rf} = \omega/\omega_{ion}$, where $\tau_{rf} = 2\pi/\omega$

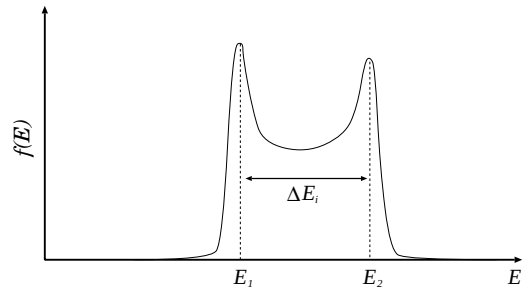

Figure 1. A bimodal ion energy distribution.

is the rf period and $\tau_{ion} = 2\pi/\omega_{ion}$ is the time an ion takes to traverse the sheath when the sheath drop is at its dc value. If we assume a collisionless Child–Langmuir space charge sheath, then the spatial variation of the sheath potential is given by

$$V_s(x) = C_1 x^{4/3} \tag{1}$$

where $C_1 = (9\bar{J}_i/(4\epsilon_0))^{2/3}(M/(2e))^{1/3}$ is independent of x, and $x = 0$ is defined at the wall. Here, $\bar{J}_i$ is the ion current density in the sheath and M is the ion mass. Also, if we neglect the initial ion velocity, then the ion velocity is given by $v(x) = (2eV_s(x)/M)^{1/2}$. So,

$$\tau_{ion} = \int_0^{\bar{s}} \frac{\mathrm{d}x}{v(x)} = \left(\frac{M}{2eC_1}\right)^{1/2} \int_0^{\bar{s}} x^{-2/3}\,\mathrm{d}x$$
$$= \left(\frac{M}{2eC_1}\right)^{1/2} 3\bar{s}^{1/3} = 3\bar{s}\left(\frac{M}{2e\bar{V}_s}\right)^{1/2} \tag{2}$$

where $\bar{s}$ is the time-averaged sheath thickness and $\bar{V}_s$ is the mean sheath voltage. Dividing by τ_{rf}, we obtain

$$\frac{\tau_{ion}}{\tau_{rf}} = \frac{3\bar{s}\omega}{2\pi}\left(\frac{M}{2e\bar{V}_s}\right)^{1/2}. \tag{3}$$

For the *low*-frequency regime ($\tau_{ion}/\tau_{rf} \ll 1$), the ions cross the sheath in a small fraction of an rf cycle and respond to the instantaneous sheath voltage. Thus, their final energies depend strongly on the phase of the rf cycle in which they enter the sheath. As a result, the IED is broad and bimodal, and the IED width ΔE_i approaches the maximum sheath drop. The two peaks in the distribution correspond to the minimum and maximum sheath drops (i.e. where the voltage is most slowly varying) (see figure 1).

For the *high*-frequency regime ($\tau_{ion}/\tau_{rf} \gg 1$), the ions take many rf cycles to cross the sheath and can no longer respond to the instantaneous sheath voltage. Instead, the ions respond only to an average sheath voltage and the phase of the cycle in which they enter the sheath becomes unimportant, resulting in a narrower IED. In this high-frequency regime, ΔE_i was calculated analytically for a collisionless sheath by Benoit-Cattin *et al* [9] and found to be directly proportional to τ_{rf}/τ_{ion}. Thus, as τ_{ion}/τ_{rf} increases, the IED width shrinks and the two peaks of the IED approach each other until, at some point, they can no longer be resolved.

2.2. Ion plasma frequency and ion transit frequency

Some authors take the natural frequency of ions in the sheath to be the ion plasma frequency ω_{pi} rather than the ion transit frequency ω_{ion}. For typical parameters, ω_{pi} and ω_{ion} may be close in value. We define the ion plasma frequency $\omega_{pi} = (n_0e^2/(\epsilon_0 M))^{1/2}$, where n_0 is the bulk plasma density, and the ion transit frequency $\omega_{ion} = 2\pi/\tau_{ion} = 2\pi(2e\bar{V}_s/M)^{1/2}/(3\bar{s})$. Then,

$$\frac{\omega_{pi}}{\omega_{ion}} = \frac{3\bar{s}}{2\pi}\left(\frac{n_0 e}{2\epsilon_0 \bar{V}_s}\right)^{1/2}. \tag{4}$$

We obtain the mean sheath width $\bar{s}$ in terms of the mean sheath voltage $\bar{V}_s$ by using the collisionless Child–Langmuir law

$$\bar{s} = \frac{2}{3}\left(\frac{2e}{M}\right)^{1/4}\left(\frac{\epsilon_0}{\bar{J}_i}\right)^{1/2}\bar{V}_s^{3/4}. \tag{5}$$

The ion current density in the sheath is given by

$$\bar{J}_i = en_s u_B \approx 0.61 n_0 u_B \tag{6}$$

where n_0 is the bulk plasma density, n_s is the ion density at the presheath–sheath boundary and $u_B = (kT_e/M)^{1/2}$ is the Bohm velocity. This implies

$$\bar{s} \approx \frac{2}{3}\left(\frac{2e}{kT_e}\right)^{1/4}\left(\frac{\epsilon_0}{0.61 n_0 e}\right)^{1/2}\bar{V}_s^{3/4} \tag{7}$$

and

$$\frac{\omega_{pi}}{\omega_{ion}} \approx \frac{0.91}{\pi}\left(\frac{2e}{kT_e}\right)^{1/4}\bar{V}_s^{1/4} \approx \frac{0.91}{\pi}\left(\frac{\bar{V}_s}{V_1}\right)^{1/4}. \tag{8}$$

For typical operating conditions, the presheath voltage drop $V_1 = kT_e/(2e) \sim 1$ V and the dc sheath voltage $\bar{V}_s \sim 100$ V so that $\omega_{pi}/\omega_{ion} \sim 1$. Thus, it is not surprising that ω_{pi} and ω_{ion} are used interchangeably in the literature. However, strictly speaking, it is ω_{ion} that determines the ion behaviour in the sheath and not ω_{pi}, which is the natural frequency of the ions in the bulk plasma.

2.3. Analytical calculation for the high-frequency regime

Benoit-Cattin *et al* [9] analytically calculated the IED and ΔE_i in the high-frequency regime ($\tau_{ion}/\tau_{rf} \gg 1$) for a collisionless rf sheath. They assumed (i) a constant sheath width, (ii) a uniform sheath electric field, (iii) a sinusoidal sheath voltage $V_s(t) = \bar{V}_s + \tilde{V}_s \sin\omega t$ and (iv) zero initial ion velocity at the plasma–sheath boundary. The resulting expressions for ΔE_i and the IED are

$$\Delta E_i = \frac{2e\tilde{V}_s}{\bar{s}\omega}\left(\frac{2e\bar{V}_s}{M}\right)^{1/2} = \frac{3e\tilde{V}_s}{\pi}\left(\frac{\tau_{rf}}{\tau_{ion}}\right) \tag{9}$$

and

$$f(E) = \frac{\mathrm{d}n}{\mathrm{d}E} = \frac{2n_t}{\omega\Delta E_i}\left[1 - \frac{4}{\Delta E_i^2}(E - e\bar{V}_s)^2\right]^{-1/2} \tag{10}$$

where n_t is the number of ions entering the sheath per unit time.

The calculations yield a bimodal IED with two peaks symmetric about $e\bar{V}_s$ and ΔE_i proportional to τ_{rf}/τ_{ion} (see figure 2). As ω or M is increased, ΔE_i is reduced and the two peaks of the IED approach each other. The two peaks

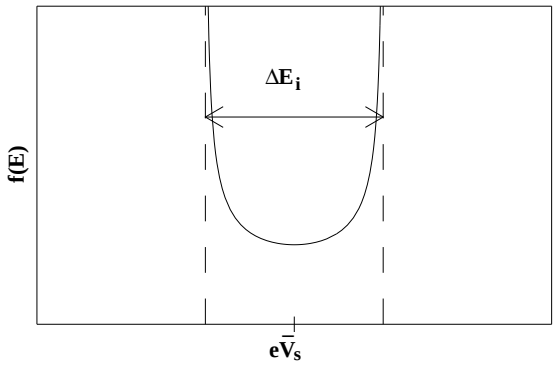

Figure 2. The analytical IED derived by Benoit-Cattin *et al* [9] for the high-frequency ($\tau_{ion}/\tau_{rf} \gg 1$) case. The singular peaks are due to the assumption of a monoenergetic initial ion velocity distribution.

of the calculated IED are singular because of the assumed monoenergetic initial velocity distribution. (See the appendix for a derivation of (9) and (10).)

In a later paper, Benoit-Cattin and Bernard [10] assumed a more realistic Child–Langmuir space-charge sheath electric field rather than a uniform sheath electric field when computing IED and ΔE_i in a collisionless rf sheath. They still only considered the high-frequency regime ($\tau_{ion}/\tau_{rf} \gg 1$) and assumed constant sheath width, sinusoidal sheath voltage and zero initial ion velocity at the plasma–sheath boundary. The expression for $f(E)$ is unchanged and the revised ΔE_i differs by just a factor of $4/3$ from the previous one:

$$\Delta E_i = \frac{8e\tilde{V}_s}{3\bar{s}\omega}\left(\frac{2e\bar{V}_s}{M}\right)^{1/2} = \frac{4e\tilde{V}_s}{\pi}\left(\frac{\tau_{rf}}{\tau_{ion}}\right). \qquad (11)$$

This slight change suggests that while the ion modulation is very important, the precise profile of the electric field in the sheath does not change the overall ion modulation result significantly.

Equations (10) and (11) show that in an rf discharge with different ion species, for each ion species, there will be two IED peaks centred at eV_s with a peak splitting which decreases with increasing ion mass. This feature can be used to crudely mass resolve experimental IEDs [25–27].

Okamoto and Tamagawa [22] did a similar calculation to Benoit-Cattin and Bernard and obtained the same ΔE_i (11). They also experimentally verified the dependence of ΔE_i on frequency ($\sim 1/f$), ion mass ($\sim M^{-1/2}$) and applied rf voltage ($\sim \tilde{V}_s$).

2.4. Analytical calculation for the low-frequency regime

We now introduce an analytical model for collisionless rf sheaths in the low-frequency regime $\tau_{ion}/\tau_{rf} \ll 1$. In this regime, the ions traverse the sheath in a fraction of the rf period and *respond to the instantaneous sheath voltage drop*. The purpose of this model is to derive analytic expressions for the voltage and current waveforms in a collisionless rf sheath in the low-frequency regime. A circuit model of the discharge is given in figure 3(a). The discharge is driven by an rf voltage source $V_0 \sin \omega t$ through a blocking capacitor C_b. We use a simple model in which the discharge is represented as the series combination of the powered electrode sheath T

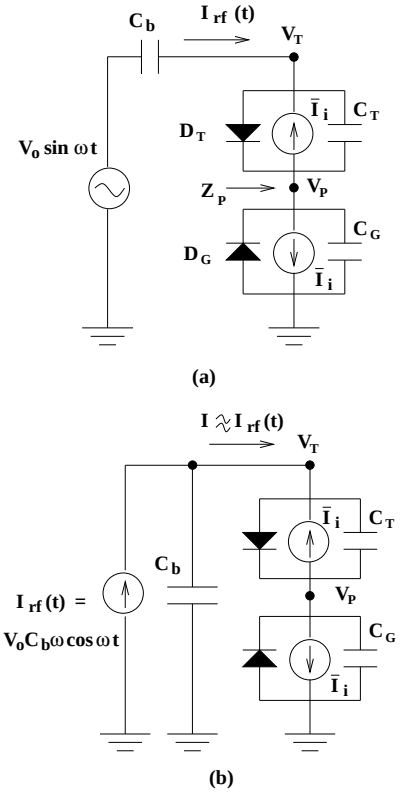

Figure 3. (a) Circuit model of discharge driven by an rf voltage source through a *large* blocking capacitor. Discharge is voltage driven. (b) Circuit model of discharge driven by an rf voltage source through a *small* blocking capacitor. Discharge is essentially current driven, and the circuit in (a) is redrawn with a Norton equivalent current source.

and the grounded electrode sheath G. Each sheath consists of the parallel combination of an ideal diode D, representing the resistive flow of electron current through the sheath to the wall, an ideal current source $\bar{I}_i$, representing the steady flow of ions, and a nonlinear capacitance C, representing the flow of displacement current. In this model the bulk plasma resistance and inductance are assumed to be negligible (point P in the figure).

Due to the blocking capacitor C_b, no dc current can flow to either electrode. This implies that the plasma potential $V_P(t)$ must be positive with respect to either electrode; otherwise, due to their greater mobility, more electrons than ions will reach the electrodes.

We will consider a symmetric reactor in which both the grounded and powered electrode have the same area A. Note that the sheath voltage at the target electrode is given by $V_{PT}(t) = V_P(t) - V_T(t)$ while the sheath voltage at the ground electrode is given by the plasma potential $V_P(t)$. Due to symmetry, we expect $V_{PT}(t)$ and $V_P(t)$ to have the same shape but be π radians out of phase with each other. We will discuss asymmetric reactors in a later section.

The low-frequency sheath capacitance can be written as

$$C_s = \frac{\mathrm{d}Q}{\mathrm{d}V_s} = \epsilon_0 A \frac{\mathrm{d}\mathcal{E}}{\mathrm{d}V_s} \qquad (12)$$

where Q is the charge on the wall, V_s is the sheath voltage

and $\mathcal{E}$ is the electric field at the wall†. For a high voltage (Child-Langmuir law) sheath $eV_s \gg kT_e$, the wall electric field is (Lieberman and Lichtenberg [38, section 6.3]):

$$\mathcal{E} = 2\left(\frac{\bar{J}_i}{\epsilon_0}\right)^{1/2}\left(\frac{MV_s}{2e}\right)^{1/4} \tag{13}$$

where the dc ion current density in the sheath $\bar{J}_i$ is given by (6). Inserting (13) and (6) into (12), we obtain

$$C_s = \frac{K}{V_s^{3/4}} \tag{14}$$

where

$$K \approx 0.327(en_0\epsilon_0)^{1/2}\left(\frac{kT_e}{e}\right)^{1/4} A. \tag{15}$$

The use of an ideal diode and current source to determine the flow of electron and ion conduction currents, and the use of the capacitance (14) to determine the displacement current, is an approximation that provides considerable insight into the sheath dynamics. More accurate expressions, valid for both low and high sheath voltages, are given by Metze *et al* [36]. (See also Lieberman and Lichtenberg [38, section 6.2].) Metze *et al*'s numerical model will be described in a later section.

2.4.1. Large blocking capacitor (figure 3(a)). There are two limiting cases depending on whether the impedance of the blocking capacitor C_b is small or large compared to the discharge impedance. For large blocking capacitors, the discharge is essentially voltage driven. In this case one or the other diode is alternately conducting and the voltages $V_P(t)$ and $V_{TP}(t)$ must sum to equal the applied voltage:

$$V_{TP} + V_P = V_0 \sin \omega t. \tag{16}$$

For ideal diodes, the conducting state has negligible voltage drops. In this approximation, the voltage across each sheath is a half-wave rectified sinusoid, as shown in figure 4(a)

$$V_P(t) = \begin{cases} V_0 \sin \omega t & 0 < \omega t \ (\mathrm{mod}\, 2\pi) < \pi \\ 0 & \pi < \omega t \ (\mathrm{mod}\, 2\pi) < 2\pi. \end{cases} \tag{17}$$

$$V_{TP}(t) = \begin{cases} 0 & 0 < \omega t \ (\mathrm{mod}\, 2\pi) < \pi \\ V_0 \sin \omega t & \pi < \omega t \ (\mathrm{mod}\, 2\pi) < 2\pi. \end{cases} \tag{18}$$

Given these voltages, the currents in the two sheath capacitors and in the circuit can be determined. For the grounded sheath, we have

$$I_{PG} = \frac{\mathrm{d}Q_{PG}}{\mathrm{d}t} = C_G \frac{\mathrm{d}V_P}{\mathrm{d}t} \tag{19}$$

which yields

$$I_{PG} = \begin{cases} \omega K V_0^{1/4} \dfrac{\cos \omega t}{(\sin \omega t)^{3/4}} & 0 < \omega t \ (\mathrm{mod}\, 2\pi) < \pi \\ 0 & \text{otherwise.} \end{cases} \tag{20}$$

† The use of $Q = CV$ is not strictly valid for a Child's law diode which has field lines ending on internal space charge as well as at the walls. See the analysis by Llewellyn in [49] which is repeated by Birdsall and Bridges in [50], where $C = 0.6C_{vac}$ at low frequencies.

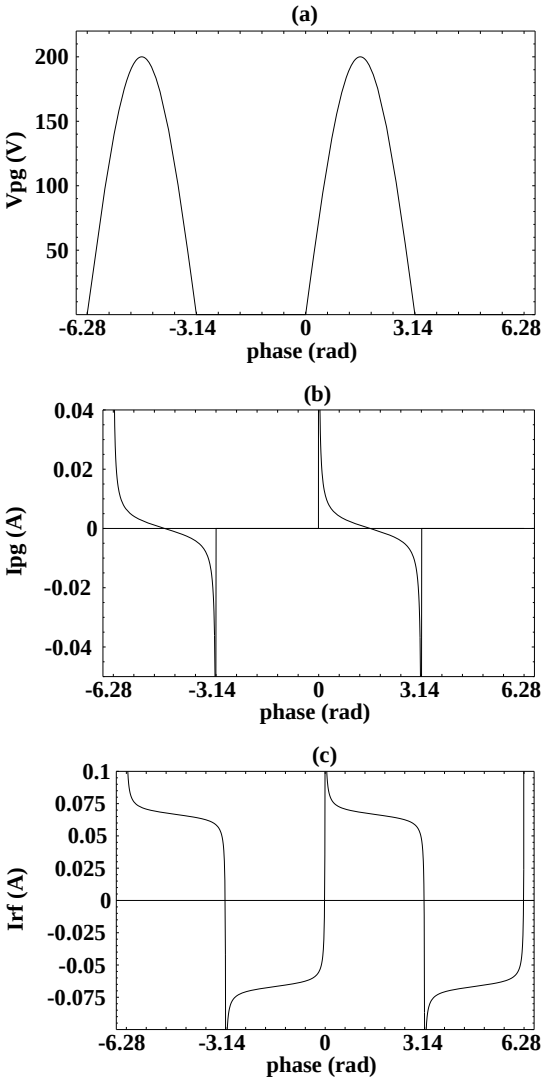

Figure 4. Results of the simple analytical model for a voltage-driven sheath: (a) sheath voltage $V_P(t)$, (b) displacement current $I_{PG}(t)$ and (c) total current $I_{rf}(t)$ versus phase ωt for $-2\pi \leqslant \omega t < 2\pi$. $V_0 = 200$ V, $C_b = 1$ F and $f = 100$ kHz.

A similar expression is found for I_{TP} for the target sheath. $I_{PG}(t)$ is plotted in figure 4(b). The singularity in (20) at $\omega t = 0, \pi \ (\mathrm{mod}\, 2\pi)$ is due to the high-voltage approximation (14) for the sheath capacitance. The singularity is integrable, which leads to non-singular behaviour for the charge Q_{PG}. This singularity is resolved in the more accurate model (Metze *et al* [36]). Summing the displacement and conduction currents, we obtain for the total currents

$$I_{rf}(t) = \begin{cases} I_{PG}(t) + \bar{I}_i = I_{PG}(t) + \bar{J}_i A \\ \qquad 0 < \omega t \ (\mathrm{mod}\, 2\pi) < \pi \\ I_{TP}(t) - \bar{I}_i = I_{TP}(t) - \bar{J}_i A \\ \qquad \pi < \omega t \ (\mathrm{mod}\, 2\pi) < 2\pi \end{cases} \tag{21}$$

as shown in figure 4(c). We compare this simple analytical model with the more accurate numerical results from the model of Metze *et al* [36] in figure 5.

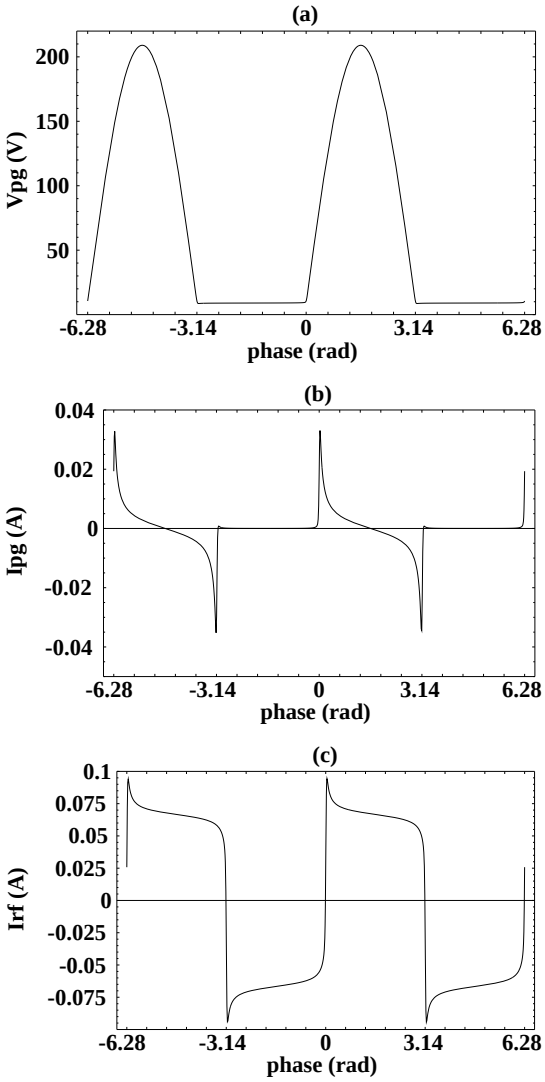

Figure 5. Results of the more accurate numerical model by Metze *et al* [36] for the voltage-driven sheath: (a) sheath voltage $V_P(t)$, (b) displacement current $I_{PG}(t)$ and (c) total current $I_{rf}(t)$ versus phase ωt for $-2\pi \leqslant \omega t < 2\pi$. $V_0 = 200$ V, $C_b = 1$ F and $f = 100$ kHz.

2.4.2. Small blocking capacitor (figure 3(b)). Now consider the opposite limit of a small blocking capacitor where the impedance of the blocking capacitor C_b is large and the discharge is essentially current driven. The circuit is redrawn by introducing a Norton-equivalent current source $I_{rf}(t) = \omega C_b V_0 \cos \omega t$, as shown in figure 3(b). We neglect the current through the blocking capacitor in figure 3(b) and first consider the ground sheath. Assuming that the ground sheath diode is open circuited, then

$$I_{PG}(t) = I_{rf}(t) - \bar{I}_i \qquad \text{diode open.} \tag{22}$$

Inserting (22) into (19) and integrating, we find

$$V_P^{1/4}(t) = \frac{V_0 C_b}{4K}[\sin\phi - \sin\phi_1 - (\phi - \phi_1)\cos\phi_1] \qquad \text{diode open} \tag{23}$$

where $\phi = \omega t$ and $\phi_1 = \omega t_1$ is the integration constant. The ground sheath changes from a short to an open circuit when

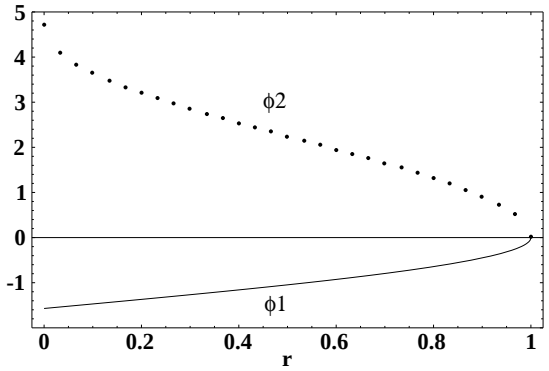

Figure 6. ϕ_2 and ϕ_1 versus r.

$I_{PG}(t)$ in (22) passes through zero, which yields

$$\phi_1 = -\cos^{-1} r \tag{24}$$

where $r = \bar{I}_i/\omega C_b V_0$ is the ratio of ion conduction current to rf current amplitude. We assume that $r < 1$ (a strongly driven system). The integration constant ϕ_1 lies in the range $-\pi/2 < \phi < 0$. The diode stays open over the time interval $\phi_1 < \phi < \phi_2$, where ϕ_2 is the phase at which the voltage V_P in (23) passes through zero. ϕ_2 is given implicitly as the solution of the equation

$$\sin\phi_2 - \sin\phi_1 = (\phi_2 - \phi_1)\cos\phi_1. \tag{25}$$

Here ϕ_2 lies in the range $0 < \phi_2 < 3\pi/2$, with $\phi_2 \approx -2\phi_1$ for $\phi_2 \ll 1$, and $\phi_2 = 3\pi/2$ for $\phi_1 = -\pi/2$. A graph of ϕ_2 and ϕ_1 versus r is given in figure 6. Hence we finally obtain the ground sheath current

$$I_{PG}(t) = \begin{cases} \omega C_b V_0(\cos\phi - \cos\phi_1) & \phi_1 < \phi < \phi_2 \\ 0 & \text{otherwise.} \end{cases} \tag{26}$$

Similarly, we obtain the sheath voltage

$$V_P^{1/4}(t) = \begin{cases} \dfrac{C_b V_0}{4K}[\sin\phi - \sin\phi_1 - (\phi - \phi_1)\cos\phi_1] \\ \qquad \phi_1 < \phi < \phi_2 \\ 0 \qquad \text{otherwise.} \end{cases} \tag{27}$$

V_P has a maximum at $\phi_{\max} = -\phi_1$, given by

$$V_{PGmax}^{1/4} = \frac{C_b V_0}{2K}(\phi_1 \cos\phi_1 - \sin\phi_1). \tag{28}$$

For $r \to 0$, such that $\phi_1 \to -\pi/2$, we find that $V_{PGmax}^{1/4} \to C_b V_0/2K$.

Similar expressions to (26) and (27) hold for the target sheath. The V_P and I_{PG} waveforms are plotted in figures 7(a) and 7(b) and the total current waveform across the discharge is shown in figure 7(c). A comparison with the results from the model of Metze *et al* [36] for this case is shown in figure 8.

Let us also note that, for $r > 1$, the diodes always remain in a short-circuited condition, and therefore the sheath voltage is zero for the ideal diode model. In this limit of low driving

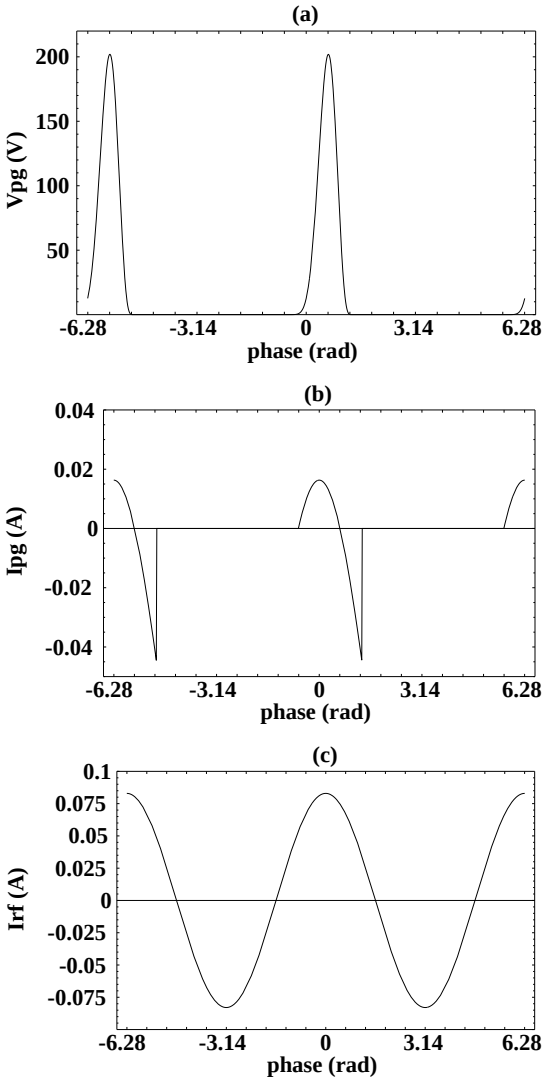

Figure 7. Results of the simple analytical model for the current-driven sheath: (a) sheath voltage $V_P(t)$, (b) displacement current $I_{PG}(t)$ and (c) total current $I_{rf}(t)$ versus phase ωt for $-2\pi \leqslant \omega t < 2\pi$. $V_0 = 6315$ V, $C_b = 20$ pF and $f = 100$ kHz.

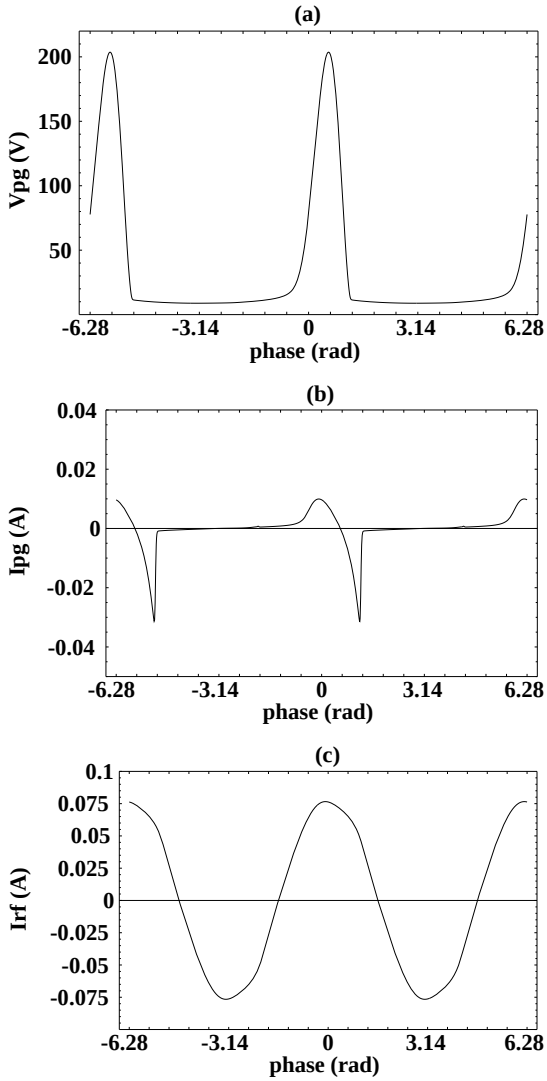

Figure 8. Results of the more accurate numerical model by Metze *et al* [36] for the current-driven sheath: (a) sheath voltage $V_P(t)$, (b) displacement current $I_{PG}(t)$ and (c) total current $I_{rf}(t)$ versus phase ωt for $-2\pi \leqslant \omega t < 2\pi$. $V_0 = 6315$ V, $C_b = 20$ pF and $f = 100$ kHz.

current, the sheath voltages actually tend toward their values for an undriven (dc) sheath:

$$V_F \approx \frac{kT_e}{2}\left(\frac{1}{2} + \ln\frac{M}{2\pi m}\right). \tag{29}$$

Let us compare the cases of large and small blocking capacitor C_b. For the large C_b case (figure 4), there is a negligible voltage drop across C_b and the discharge is voltage driven. The total voltage drop $V_T(t) = V_{TP}(t) + V_P(t)$ across the discharge equals the drive voltage $V_0 \sin\omega t$ and is sinusoidal. However, the total current $I_{rf}(t)$ across the discharge is non-sinusoidal. In contrast, for the small C_b case (figure 7), there is a significant voltage drop across C_b and the discharge is current driven. The total current $I_{rf}(t)$ across the discharge equals $\omega C_b V_0 \cos\omega t$ and is sinusoidal. However, the total voltage drop $V_T(t)$ across the discharge is non-sinusoidal. But, in both cases, the voltage drop across each *sheath* ($V_P(t)$ or $V_{PT}(t)$) is non-sinusoidal and resembles a half-wave rectified signal.

From the above analytical model, we see that, in the low-frequency regime ($\tau_{ion}/\tau_{rf} \ll 1$), the voltage drops across the sheaths are non-sinusoidal due to the nonlinear properties of the sheath capacitances and the conduction currents. The sheath voltages are at a minimum value for a longer portion of the rf cycle than at a maximum value. This implies that ions are accelerated by a small potential drop for a larger fraction of the rf cycle than for a large potential drop. This effect results in IEDs with dominant low-energy peaks. The more accurate numerical model of Metze *et al* [36] shows similar results.

2.5. Ion energy distribution at the electrodes

Since the sheath voltage waveform is periodic, the energy E of an ion hitting the target depends on the phase angle ωt_0 at which the ion enters the sheath. Thus, if $P(E)\,\mathrm{d}E$ is the fraction of ions hitting the target with energies between E and

$E + \mathrm{d}E$, and $P(\omega t_0)\,\mathrm{d}(\omega t_0)$ is the fraction of ions entering the sheath during the phase angles ωt_0 and $\omega t_0 + \mathrm{d}(\omega t_0)$, then $P(E)\,\mathrm{d}E = P(\omega t_0)\,\mathrm{d}(\omega t_0)$ or

$$P(E) = P(\omega t_0)\left|\frac{\mathrm{d}E}{\mathrm{d}(\omega t_0)}\right|^{-1}. \tag{30}$$

For both the low-and high-frequency regimes, we can assume that the flux of ions entering the sheath from the presheath is a constant: $\Gamma_i = n_s u_B = \text{constant}$. For the low-frequency case, this is true because the sheath motion is slow compared to the Bohm velocity u_B. For the high-frequency case, this is true because the ions see a constant time-averaged sheath width. So, $P(\omega t_0) = 1/(2\pi)$ for both the low- and high-frequency regimes. This implies that for the low- and high-frequency regimes

$$P(E) = \frac{1}{2\pi}\left|\frac{\mathrm{d}E}{\mathrm{d}(\omega t_0)}\right|^{-1}. \tag{31}$$

Furthermore, for the low-frequency regime, we have

$$E(\omega t_f) \approx E(\omega t_0) \approx eV_s(\omega t_0) \tag{32}$$

where $t_f - t_0$ is the ion transit time across the sheath, so that

$$P(E) = \frac{1}{2e\pi}\left|\frac{\mathrm{d}V_s}{\mathrm{d}(\omega t_0)}\right|^{-1}_{V_s=E/e}. \tag{33}$$

Therefore, for the low-frequency regime, given the sheath voltage waveform $V_s(t)$, we can deduce the IEDs.

As an example, let us derive $P(E)$ for the case of the voltage-driven low-frequency symmetric rf reactor described in the previous section. From (17) and (32), we have

$$E(\omega t_0) = \begin{cases} eV_0 \sin\omega t & 0 < \omega t_0 < \pi \\ 0 & \pi < \omega t_0 < 2\pi. \end{cases} \tag{34}$$

For $0 < \omega t_0 < \pi$,

$$\frac{\mathrm{d}V_s}{\mathrm{d}(\omega t_0)} = V_0 \cos\omega t_0 = V_0(1 - \sin^2\omega t_0)^{\frac{1}{2}}. \tag{35}$$

Noting that there are two values of ωt_0 during one rf cycle for each value of E, we have for $0 < \omega t_0 < \pi$,

$$\begin{aligned} P(E) &= \frac{1}{e\pi}(V_0^2 - V_0^2\sin^2\omega t_0)^{-\frac{1}{2}} \\ &= \frac{1}{\pi}((eV_0)^2 - E^2))^{-\frac{1}{2}} \qquad 0 < E < eV_0. \end{aligned} \tag{36}$$

For $\pi < \omega t_0 < 2\pi$ (an interval of $\Delta(\omega t_0) = \pi$), $E(\omega t_0) = eV_s(\omega t_0) = 0$, and (31) yields

$$P(E) = \frac{\pi}{2\pi}\delta(E) = \frac{1}{2}\delta(E). \tag{37}$$

The total IED is the sum of (36) and (37). The distribution is broad and independent of ion mass since, in the low-frequency regime, all ions of any mass respond to the full range of the slowly varying $V_s(t)$. The distribution is singular (but integrable) at the peaks due to the assumption of monoenergetic initial velocity distribution.

If an energy analyser has a finite energy resolution of width ΔE, then an experiment will actually measure

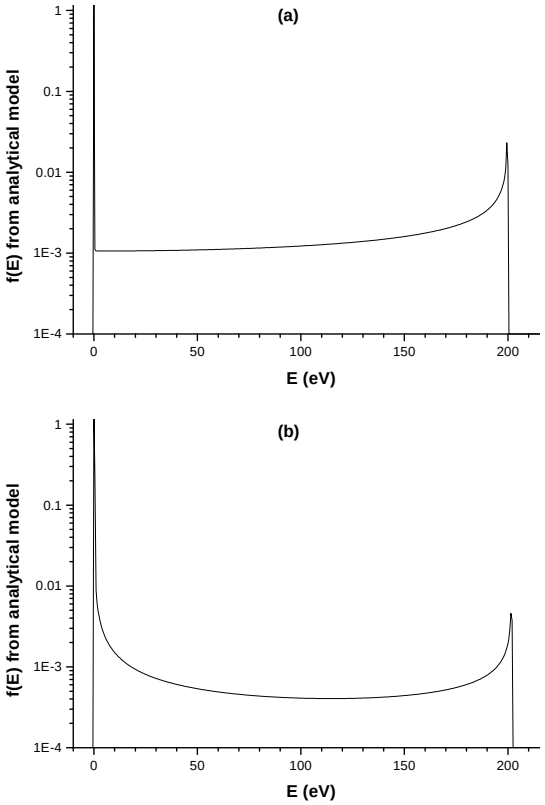

Figure 9. IEDs derived from the analytical model. (a) From the voltage-driven case; (b) from the current-driven case.

$\bar{P}(E)$, the average of $P(E)$ over the energy window ΔE. Expressions (17) and (28) for $V_s(t)$ in the voltage- and current-driven cases, respectively, can be used to find $\bar{P}(E)$ for the analytical low-frequency regime model (see figure 9). These can be compared with the IEDs derived from the voltage waveforms of the more accurate Metze *et al* [36] model (see figure 10). For both figures, we plot $\bar{P}(E)$ assuming a rectangular window with $\Delta E = 0.5$ eV. As expected, the IEDs have dominant low-energy peaks because in the low-frequency regime $V_s(t)$ is at a minimum value for a longer fraction of the rf cycle than it is at a maximum value. In contrast to the analytical model, the Metze *et al* model takes the finite dc sheath floating potential V_F (29) into account so that the lowest value of ion impact energy E is eV_F rather than zero.

2.6. Sheath impedance, resistive or capacitive

Whether or not the high-energy peak or low-energy peak of the IED dominates at low τ_{ion}/τ_{rf} depends on whether or not the sheath voltage $V_s(t)$ is mostly at a maximum or minimum during an rf cycle. The sheath voltage waveform depends strongly on the nature of the sheath, i.e. whether it is resistive or capacitive. A sheath is resistive if $J_c \gg J_d$ and it is capacitive if $J_c \ll J_d$, where J_c is the conduction current density and J_d is the displacement current density.

As a rough approximation, let us neglect the contribution of the electrons to the conduction current density. This implies that $J_c \approx \bar{J}_i$, where $\bar{J}_i$ is the ion current density across

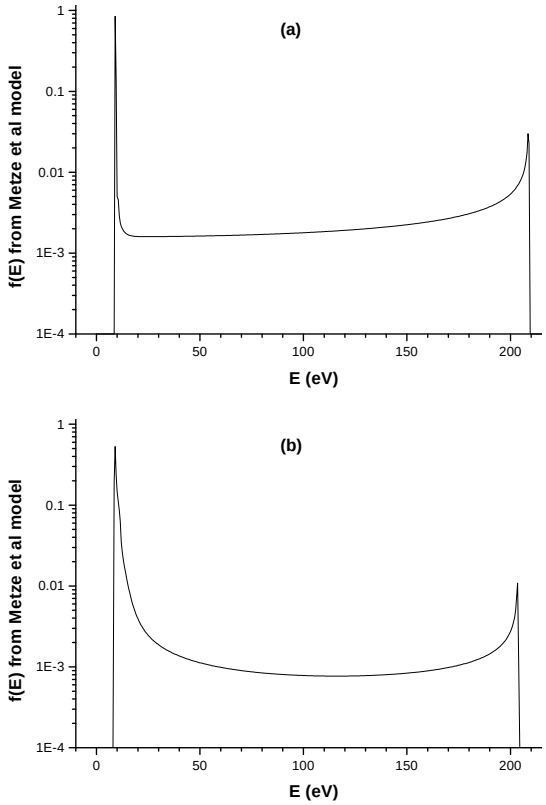

Figure 10. IEDs derived from the Metze *et al* [36] model. (a) From the voltage-driven case; (b) from the current-driven case.

the sheath. For a collisionless Child–Langmuir sheath, the ion current density is given by

$$\bar{J}_i = \frac{4\epsilon_0}{9}\left(\frac{2e}{M}\right)^{1/2}\frac{\bar{V}_s^{3/2}}{\bar{s}^2}. \tag{38}$$

Let a displacement current magnitude be defined by

$$J_d = \frac{\omega\tilde{V}_s\epsilon_0}{\bar{s}}. \tag{39}$$

This implies that

$$\frac{J_c}{J_d} \approx \frac{2\tau_{rf}}{9\pi\bar{s}}\left(\frac{\bar{V}_s}{\tilde{V}_s}\right)\left(\frac{2e\bar{V}_s}{M}\right)^{1/2}. \tag{40}$$

Finally, by using $\tau_{ion} = 3\bar{s}(M/(2e\bar{V}_s))^{1/2}$, we see that for a collisionless sheath

$$\frac{J_c}{J_d} \approx 0.2\left(\frac{\bar{V}_s}{\tilde{V}_s}\right)\left(\frac{\tau_{rf}}{\tau_{ion}}\right). \tag{41}$$

For a high voltage sheath with $\bar{V}_s \sim \tilde{V}_s$, $J_c/J_d \sim \tau_{rf}/\tau_{ion}$. Thus, if $\tau_{ion}/\tau_{rf} \gg 1$, the sheath tends to be capacitive, whereas, if $\tau_{ion}/\tau_{rf} \ll 1$, the sheath tends to be resistive.

For a capacitive sheath driven by a sinusoidal target potential $V_T(t)$, the plasma potential $V_P(t)$ is nearly sinusoidal so that the target sheath voltage $V_s(t) = V_P(t) - V_T(t)$ is also nearly sinusoidal. Due to the symmetry in $V_s(t)$, the fraction of the rf cycle in which $V_s(t)$ is at a minimum value is equal to the fraction of the rf cycle in which it is at a maximum value. As a result, the two peaks of the bimodal collisionless IEDs are more or less of equal height.

For a resistive sheath, the plasma potential $V_P(t)$ is non-sinusoidal even when the sheath is driven by a sinusoidal target potential $V_T(t)$. In general, for resistive sheaths, $V_P(t)$ follows the positive excursions of $V_T(t)$ and resembles a half-wave rectified signal clipped at the floating potential V_F. Thus, the target sheath voltage $V_s(t) = V_P(t) - V_T(t)$ is non-sinusoidal and at a minimum value for a longer fraction of the rf period than it is at a maximum value. As a result, the bimodal collisionless IEDs have a dominant low-energy peak at energy $E = eV_F$.

Hence as τ_{ion}/τ_{rf} increases, we see a transition from a low-frequency ($\tau_{ion}/\tau_{rf} \ll 1$), resistive ($J_c/J_d \gg 1$) sheath with a broad bimodal IED and a dominant low-energy peak to a high-frequency ($\tau_{ion}/\tau_{rf} \gg 1$), capacitive ($J_c/J_d \ll 1$) sheath with a narrow bimodal IED and peaks of more or less equal height.

2.7. Asymmetric discharges and bias voltages

In section 2.4, we analysed a symmetric capacitively coupled rf reactor in which the grounded electrode area A_G is equal to the driven target electrode area A_T. Due to symmetry, the sheath voltage waveform $V_P(t)$ at the grounded electrode and the sheath voltage waveform $V_{PT}(t)$ at the target electrode had the same shape but were π radians out of phase with each other. Also, $V_P(t)$ was positive with respect to either electrode to ensure that no dc current flowed to the electrodes; otherwise, because of their greater mobility, many more electrons than ions would reach the electrodes.

However, most capacitively coupled reactors are asymmetric ($A_G > A_T$) since more electrode surfaces are grounded rather than driven. In this case, not only must the plasma be biased positive with respect to either electrode, but the smaller electrode must be biased negative with respect to the larger electrode to ensure zero dc current.

Figure 11(a) is the model of a low-frequency voltage-driven asymmetric capacitively coupled rf reactor proposed by Song *et al* [37]; the discharge density n_0 is assumed to be uniform while the sheaths are assumed to be collisionless and resistive. In figure 11(b), we introduce an equivalent circuit model. The purpose of this model is to simplify the calculations made by Song *et al* in deriving the voltage drop across each sheath and the bias voltage between the electrodes.

Here, $\bar{I}_{iG} = en_0u_BA_G$ and $\bar{I}_{iT} = en_0u_BA_T$ are the ion conduction currents in the grounded sheath and target sheath, respectively. The diodes represent the resistive flow of electrons to the electrodes. The circuit model is similar to figure 3(a) for the voltage-driven, low-frequency analytical model except that it ignores the sheath capacitances and displacement currents. This approximation is valid in a low-frequency regime where the sheath conduction currents dominate sheath displacement currents (i.e. resistive sheaths).

Both $V_P(t)$ and $-V_{PT}(t) = V_{TP}(t)$ are plotted in figure 12(a). Since the plasma must always be positive with respect to the electrodes, $V_P(t)$ and $V_{PT}(t)$ are never negative. Instead, the sheaths are rectifying, and $V_P(t)$ and $V_{PT}(t)$ are alternately positive and clamped near zero.

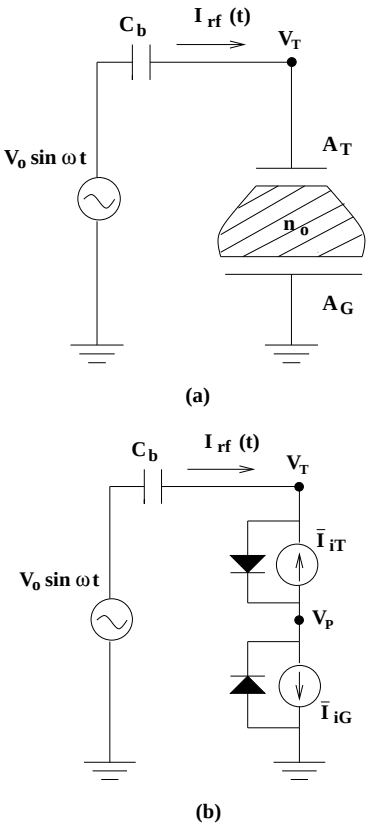

Figure 11. (a) The model of an asymmetric rf discharge. (b) The equivalent circuit model of an asymmetric rf discharge with resistive sheaths.

The electron currents can reach the electrodes only when the sheath voltages are near zero. Thus, one or the other sheath alternately limits the current to that of the ions alone. As a result, the total current $I_{rf}(t)$ has the square wave shape shown in figure 12(b). Let Δt_T and Δt_G, as shown in figure 12(a), be the time intervals for electron collection by the target and grounded electrodes, respectively. The blocking capacitor (C_b in figure 11) ensures that $I_{rf}(t)$ has no dc component. Then from figure 12(b), we must have $en_0u_BA_G\Delta t_T = en_0u_BA_T\Delta t_G$ or

$$\frac{\Delta t_T}{\Delta t_G} = \frac{A_T}{A_G} < 1. \tag{42}$$

Δt_G can be eliminated by using $\Delta t_T + \Delta t_G = 2\pi/\omega$ to obtain

$$\omega\Delta t_T = 2\pi\frac{A_T}{A_T + A_G}. \tag{43}$$

In order to get $\Delta t_T/\Delta t_G < 1$, a dc self-bias voltage V_{bias} builds up between the electrodes so that

$$V_T(t) = V_P(t) - V_{PT}(t) = V_0\sin\omega t - |V_{bias}|. \tag{44}$$

From figure 12(a) with $V_T(t)$ given by (44), we see that $V_T(t_1) = V_0\sin\omega t_1 - |V_{bias}| = 0$ or

$$\omega t_1 = \sin^{-1}(|V_{bias}|/V_0). \tag{45}$$

Also from figure 12(a) and (44), we see that $V_T(t_1) = V_0\sin\omega t_1 - |V_{bias}| = V_T(t_2) = V_0\sin\omega t_2 - |V_{bias}|$ so that

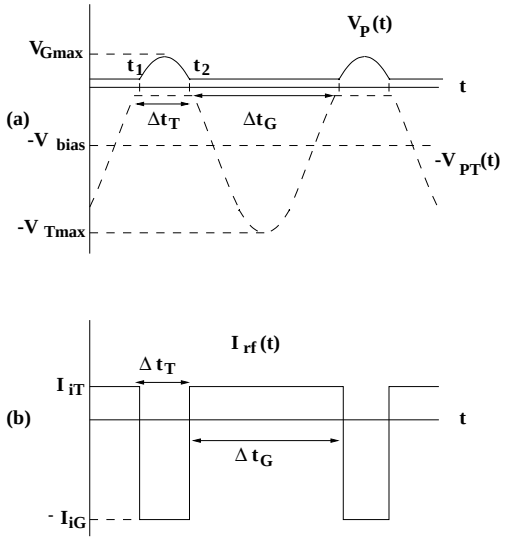

Figure 12. (a) Sheath voltage waveforms and (b) rf current of an asymmetric rf discharge with $A_G/A_T = 3$.

$\sin\omega t_1 = \sin\omega t_2$. Since, $\sin\omega t_1 = \sin\omega(\pi - \omega t_1)$, we also have

$$\omega t_2 = \pi - \omega t_1. \tag{46}$$

Combining (45) with (46), we obtain

$$\omega\Delta t_T = \omega(t_2 - t_1) = (\pi - \omega t_1) - \omega t_1$$
$$= \pi - 2\sin^{-1}(|V_{bias}|/V_0). \tag{47}$$

Equating (43) to (47) and solving for $|V_{bias}|$, we obtain

$$|V_{bias}| = V_0\sin\left(\frac{\pi}{2}\frac{A_G - A_T}{A_G + A_T}\right). \tag{48}$$

The maximum potentials at the target and grounded electrodes are $V_{Tmax} = V_0 + |V_{bias}|$ and $V_{Gmax} = V_0 - |V_{bias}|$, respectively. Using (48) it can be shown that for A_G/A_T not far from unity (e.g. $A_G/A_T \lesssim 5$),

$$\frac{V_{Tmax}}{V_{Gmax}} \approx \left(\frac{A_G}{A_T}\right)^{\pi/2}. \tag{49}$$

Equation (49) which has a scaling factor of $\pi/2$ is in closer agreement with many experiments than an earlier high-frequency analysis by Koenig and Maissel [40], which gave a scaling factor of 4. Note that for a symmetric discharge with $A_G = A_T$, $V_{bias} = 0$ and the maximum target sheath voltage $V_{Tmax} = V_0$, while for a very asymmetric discharge with $A_G \gg A_T$, $|V_{bias}| = V_0$ and $V_{Tmax} = V_0 + V_{bias} = 2V_0$.

In a related paper (Field *et al* [14]), the sheath voltage waveforms derived by Song *et al* were used to calculate the IEDs at the smaller electrode of a capacitively coupled asymmetric rf reactor. The spatial variation of the sheath potential was assumed to follow the collisionless Child–Langmuir law (1). Monte Carlo techniques were employed to follow the ion trajectories in a time-varying sheath. The ions were directed toward the target electrode at a randomly chosen rf phase from a fixed plane of origin $x = l_{max}$ greater than the maximum sheath width. The initial ion velocities were randomly chosen from a Maxwellian distribution with temperature T_i. Field *et al* calculated

IEDs at frequencies of 100 kHz and 13.56 MHz. (Strictly speaking, the low-frequency regime voltage waveforms derived by Song *et al* were not valid at the higher frequency of 13.56 MHz.) They obtained the familiar collisionless bimodal IEDs. At the higher frequency, the peak splitting was narrower and the peaks were more equal in height.

2.8. Analytical model for the intermediate-frequency regimes

So far, we have seen that in the low-frequency resistive regime the collisionless IED is broad and bimodal with a dominant low-energy peak. As τ_{ion}/τ_{rf} increases, the peak splitting ΔE_i narrows systematically and the two peaks become more equal in height. However, we often see an asymmetry in the peak heights even when the sheath is not resistive but approaches the capacitive case (e.g $\tau_{ion}/\tau_{rf} > 1$ but not much greater than 1). Sometimes the asymmetry favours the high-energy peak.

Farouki *et al* [11] used an idealized analytical model of the collisionless rf sheath in order to extract the qualitative features of IEDs. In their model, they assumed a sinusoidally oscillating plasma–sheath boundary. Between the electrode and the plasma–sheath boundary, the electric field is uniform; outside this region, it is zero. The extent of the sheath is given by $-d \leqslant x \leqslant d$, with the plasma–sheath boundary described by $x_s(t) = -d\cos(\omega t+\phi)$, where ϕ is the phase of the sheath oscillation at the time $t = 0$ when an ion enters the sheath. All the ions enter the sheath from the plasma with initial speed u_B and initial position $x = -d$. The ions impinge on the target electrode at $x = +d$. The monoenergetic incoming ion flux is assumed to be independent of the phase of the rf cycle. The ion equation of motion is given by

$$\frac{\mathrm{d}^2x}{\mathrm{d}t^2} = \frac{e\bar{V}_s}{Md}H[x - x_s(t)] \tag{50}$$

where $H(z) = 1$ if $z \geqslant 0$ and $H(z) = 0$ otherwise. Thus, an ion travelling toward the electrode experiences an alternating sequence of constant-velocity and constant-acceleration intervals as the oscillating plasma–sheath boundary intersects its path. The dimensionless parameters $\alpha = e\bar{V}_s/(M\omega^2d^2) \sim (\tau_{rf}/\tau_{ion})^2$ and $\beta = u_B/(\omega d)$ govern the ion trajectories.

In the low-frequency limit, the model yields a broad bimodal IED with singular but integrable peaks at $E = E_{min} = Mu_B^2/2$ and $E = E_{max} = E_{min} + 2e\bar{V}_s$. In the high-frequency limit, all the ions arrive at the electrode with energy $e\bar{V}_s$, resulting in a δ-function IED centred at $E = e\bar{V}_s$. This simple model yields the expected qualitative features. At very low frequencies, the IED is broad, bimodal and peaked at the smallest and largest possible ion bombarding energies. At very high frequencies, the IED is singly peaked at $e\bar{V}_s$.

In the intermediate-frequency regime, the ion trajectory for a given ϕ depends on the number of times the oscillating plasma–sheath boundary crosses the ion's path. The resulting energy distributions are bimodal. Ions in the high-energy peak generally have one less encounter with the sheath field than ions in the low-energy peak. The former group of ions have a longer unimpeded final run in the field before hitting the electrode. As the rf frequency is increased, Farouki *et al* observed a systematic narrowing of the IEDs but the precise shapes of the IEDs exhibited rapid variations; they observed a 'quasiperiodic' behaviour in the relative prominence of the low- and high-energy peaks.

3. Numerical models of the collisionless rf sheath

3.1. Numerical model for the low-frequency regime

Metze *et al* [36] presented a numerical model for a collisionless planar rf plasma reactor operating in the low-frequency regime. Unlike the low-frequency analytical model described in section 2.4, this numerical model is valid for both high and low sheath voltages. Besides $\tau_{ion}/\tau_{rf} \ll 1$, Metze *et al* assumed: (i) the electrons and ions had Maxwellian velocity distributions inside the plasma with constant in time temperatures of T_e and T_i, respectively ($T_i \ll T_e$); (ii) the electrons had a Boltzmann density distribution in the presheath and sheath; (iii) the electric field was zero at the boundary between the bulk plasma and the presheath; (iv) ions entered the sheath from the presheath at the Bohm velocity $u_B = (kT_e/M)^{\frac{1}{2}}$.

Figure 13(a) illustrates the electron and ion conduction currents and the displacement current that flow through an rf sheath. In the model, the potential $\phi(x)$ at a position x within the sheath is negative because the zero of potential is chosen to be at the plasma. A presheath voltage drop $V_1 = -kT_e/(2e)$ accelerates an ion from the near zero velocities in the bulk plasma to u_B. The ion conduction current density $\bar{J}_i$ in the sheath is given by (6). The electron conduction current density J_e in the sheath is given by $J_e(V_s) = -(en_0\bar{v}_e/4)\exp(eV_s/(kT_e))$, where $\bar{v}_e = [8kT_e/(\pi m)]^{\frac{1}{2}}$ is the mean speed of the electrons. Figure 13(b) shows the equivalent circuit model for the rf reactor proposed by Metze *et al* [36]. For the target sheath, $V_s = V_T - V_P$ while for the ground sheath $V_s = -V_P$. Thus, the total conduction currents reaching the target and ground electrodes are given by

$$\begin{aligned} I_T &= A_T[\bar{J}_i + J_e(V_T - V_P)] \\ &= A_T en_0\left[u_B\exp\left(-\frac{1}{2}\right) - \frac{1}{4}\bar{v}_e\exp\left(e\frac{V_T - V_P}{kT_e}\right)\right] \\ I_G &= A_G[\bar{J}_i + J_e(-V_P)] \\ &= A_G en_0\left[u_B\exp\left(-\frac{1}{2}\right) - \frac{1}{4}\bar{v}_e\exp\left(-e\frac{V_P}{kT_e}\right)\right]. \end{aligned} \tag{51}$$

The displacement current is given by

$$I_d = \frac{\mathrm{d}Q}{\mathrm{d}t} = \frac{\mathrm{d}Q}{\mathrm{d}V_s}\frac{\mathrm{d}V_s}{\mathrm{d}t} \equiv C_s\frac{\mathrm{d}V_s}{\mathrm{d}t} \tag{52}$$

where Q is the surface charge on the electrode and C_s is the sheath capacitance. For a planar electrode of area A and electric field $\mathcal{E}$ at the surface,

$$C_s = \frac{\mathrm{d}Q}{\mathrm{d}V_s} = -\epsilon_0\int\frac{\partial\mathcal{E}}{\partial V_s}\mathrm{d}A = -\epsilon_0 A\frac{\partial\mathcal{E}}{\partial V_s}. \tag{53}$$

From (i) the ion continuity equation $n_su_B = n_i(x)v_i(x)$, (ii) energy conservation $Mv_i(x)^2/2 + e\phi(x) = 0$ and (iii) Poisson's equation $\mathrm{d}^2\phi/\mathrm{d}x^2 = (e/\epsilon_0)[n_i - n_0\exp(e\phi(x)/(kT_e))]$, we obtain

$$\mathcal{E} = -\sqrt{\frac{2n_skT_e}{\epsilon_0}}\left[\exp\left(\frac{e(V_s - V_1)}{kT_e}\right) + \sqrt{\frac{V_s}{V_1}} - 2\right]^{\frac{1}{2}}. \tag{54}$$

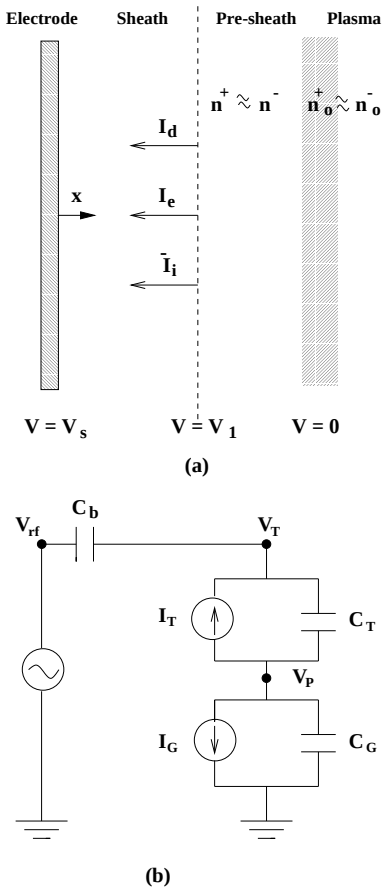

Figure 13. (a) A schematic representation of a sheath near an electrode from Metze *et al* [36]. (b) The equivalent circuit model of an rf sheath from Metze *et al* [36].

The sheath capacitances $C_s(V_s)$ are obtained by inserting (54) into (53). The target sheath capacitance is given by $C_T = C_s(V_T - V_P)$ while the ground sheath capacitance is given by $C_G = C_s(-V_P)$. Kirchhoff's current law applied to the equivalent circuit model in figure 13(b) yields

$$0 = C_b \frac{\mathrm{d}}{\mathrm{d}t}(V_{rf} - V_T) + C_T \frac{\mathrm{d}}{\mathrm{d}t}(V_P - V_T) + I_T$$

$$0 = C_T \frac{\mathrm{d}}{\mathrm{d}t}(V_P - V_T) + I_T + C_G \frac{\mathrm{d}}{\mathrm{d}t} V_P + I_G. \qquad (55)$$

The set of circuit equations together with the expressions for C_T, C_G, I_T and I_G were solved numerically to obtain the voltage waveforms $V_T(t)$ and $V_P(t)$. The results of this model have already been seen for a voltage-driven and current-driven symmetric ($A_T = A_G$) rf reactor in figures 5 and 8, respectively. The sheath voltage drops are half-wave rectified signals clamped at the floating voltage. This is typical for sheaths in the low-frequency resistive regime. Since the sheath drop is at a minimum value for a longer portion of the rf cycle than at a maximum value, the resulting bimodal IEDs have dominant low-energy peaks as previously seen in figure 10. Metze *et al* also simulated asymmetric rf reactors and found (as in section 2.7) that a dc self-bias voltage developed between the electrodes so that the smaller electrode was negatively biased with respect to the larger electrode.

In a related paper, Metze *et al* [13] used the sheath voltage waveforms obtained from their equivalent circuit model to determine the IEDs for rf frequencies of 100 kHz and 13.56 MHz in an rf argon plasma reactor. Strictly speaking, their model was not valid at the higher frequency of 13.56 MHz because the argon ions in the rf reactor they modelled could not respond to the instantaneous sheath voltage drop at frequencies higher than about 1 MHz. Metze *et al* saw bimodal IEDs in which the peak splitting decreased as frequency (or τ_{ion}/τ_{rf}) increased. They also observed that for low frequencies (or $\tau_{ion}/\tau_{rf} \ll 1$), the IEDs had dominant low-energy peaks.

3.2. Numerical model for the intermediate frequency regime

The rf sheath model developed by Metze *et al* is valid only in the low-frequency regime where the ions are essentially inertialess and respond to the instantaneous sheath voltage drop. A generalization of this model which includes ion inertia and is valid for a broad range of frequencies was proposed by Riley [41, 42]. As in the Metze *et al* model, the electrons are assumed to be inertialess with a Boltzmann distribution in the sheath. The ions in the model are assumed to respond to a damped potential $V_d(x,t)$ which is derived from the actual instantaneous potential $V(x,t)$ by a relaxation relation.

$$\dot{V}_d(x,t) = -(V_d(x,t) - V(x,t))/\tau_{ion}. \qquad (56)$$

The ion transit time across the sheath τ_{ion} controls the ion's response in the rf field. If $\tau_{ion}/\tau_{rf} \ll 1$, then the damped potential V_d approaches the actual potential V and the ions are inertialess. If $\tau_{ion}/\tau_{rf} \gg 1$, then the damped potential V_d approaches the true time average of the actual potential V and the ions are inertial.

The use of the damped potential V_d does not affect the ion continuity equation, $n_i(x,t) = n_i(x_0,t)v_i(x_0,t)/v_i(x,t)$, where x_0 is some reference point within the plasma. However, the ion energy conservation equation is now given by $m_i v_i^2(x,t)/2 + eV_d(x,t) = m_i v_i^2(x_0,t)/2 + eV_d(x_0,t)$. These two equations are combined to obtain the ion density,

$$n_i(x,t) = n_i(x_0,t)\left[1 - \frac{2e}{m_i v_i^2(x_0,t)}(V_d(x,t) - V_d(x_0,t))\right]^{-1/2}. \qquad (57)$$

In the Metze *et al* model, the first integral of the Poisson equation was solved to obtain the electric field as a function of potential. This, in turn, enabled the calculation of the displacement currents in the sheath. However, for the generalized sheath model, an exact first integral of the Poisson equation, $V'' = (e/\epsilon_0)(n_i - n_e)$, cannot be obtained because of the dependence of n_i on the damped potential V_d. Instead, an approximate solution is obtained by assuming that V and V_d are related by a function only of the time variable: $V_d(x,t) \approx \alpha(t)V(x,t)$.

Riley tested his generalized sheath model in both the low- and high-frequency limits. For $\tau_{ion} = \tau_{rf}/1000$, the calculated sheath voltage waveform was close to the one obtained by the low-frequency model of Metze *et al*.

For $\tau_{ion} = 10\tau_{rf}$, the calculated sheath voltage waveform was close to the one obtained by an analytic high-frequency sheath model developed by Lieberman [39].

In a related paper, Miller and Riley [43] compared the predictions of the generalized sheath model with experiment for an rf argon discharge operated at 13.56 MHz. They found substantial agreement between the predicted and measured rf sheath voltage, current and power. The numerical model was used to calculate sample IEDs for varying inductances and capacitances in the external circuit while keeping the frequency and power fixed. The calculated IEDs were bimodal, the low-energy peak did not vary much with variations in the external circuit. However, the high-energy peak shifted when the external circuit components were varied. One possible explanation is that the IEDs were calculated in a low-frequency regime. In this case, the low-energy peak is determined by the floating potential V_F (29) which is a function of the electron temperature and the ratio of the ion and electron masses, whereas the high-energy peak is determined by the maximum sheath voltage drop which is sensitive to external circuit parameters.

3.3. Numerical model with constant sheath width

Tsui [12] numerically integrated the equations of motion in order to obtain IEDs in a collisionless rf sheath for τ_{ion}/τ_{rf} ranging from about 1 to 20 (intermediate- to high-frequency regimes). He noted the dependence of IEDs on the parameter $a_i = 8e\bar{V}_s/(M\omega^2\bar{s}^2) \approx (\tau_{rf}/\tau_{ion})^2$. Tsui calculated IEDs for a_i in the range of 0.526 to 2.64×10^{-3} which corresponds to τ_{ion}/τ_{rf} in the range of about 1 to 20.

In his calculations, he assumed (i) a constant sheath width, (ii) a spatially linearly-varying sheath electric field, (iii) a sinusoidal sheath voltage, (iv) $T_i = T_e$, where T_i and T_e are the bulk plasma ion and electron temperatures, and (v) a Maxwellian initial ion velocity distribution at the sheath edge with $v_{th} = (kT_i/M)^{1/2}$. In general, $T_i \ll T_e$, so that assumption (iv) is invalid. However, this assumption did not affect the overall results, since in Tsui's calculations T_i is important only in determining the initial ion velocity distribution; and, for final velocity v_f much greater than the initial velocity v_0 (the usual case), the IEDs are insensitive to initial ion velocities. Also, although the assumption of sinusoidal sheath voltage (assumption (iii)) is valid in the high-frequency regime, it is not strictly true in the intermediate-frequency regime.

As shown in figure 14, Tsui also saw bimodal IEDs centred at $e\bar{V}_s$. For lower a_i (e.g. $a_i = 2.64 \times 10^{-3}$ or $\tau_{ion}/\tau_{rf} \approx 20$), the IEDs became narrower and the peaks became more equal in height. For higher a_i (e.g. $a_i = 0.526$ or $\tau_{ion}/\tau_{rf} \approx 1$), the IEDs became wider and the low-energy peak disappeared. Since Tsui did not look at $a_i \gg 1$, he had no calculations of IEDs in the low-frequency regime $\tau_{ion}/\tau_{rf} \ll 1$.

The unexpected disappearance of the low-energy peak for higher a_i (lower τ_{ion}/τ_{rf}) is due to Tsui's assumption of constant sheath width. If $\tau_{ion}/\tau_{rf} < 1$, the ions traverse the sheath in a fraction of the rf cycle. If sheath width oscillation is taken into account, the low-energy ions which enter the sheath near a minimum voltage see a shorter sheath

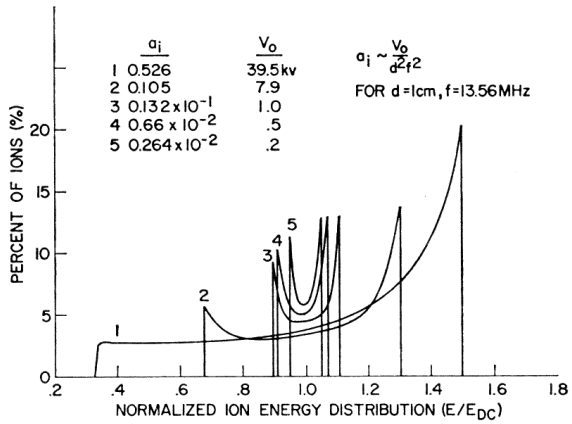

Figure 14. IEDs from Tsui [12] for different values of $a_i \approx (\tau_{rf}/\tau_{ion})^2$. The unexpected disappearance of the low-energy peak at higher a_i (lower τ_{ion}/τ_{rf}) is due to Tsui's assumption of constant sheath width.

width than the high-energy ions which enter the sheath near a maximum voltage. Due to their shorter path, low-energy ions can traverse the sheath without seeing a significant voltage spread while, due to their greater acceleration, high-energy ions can also cross the sheath without seeing a significant voltage spread. However, if we assume constant sheath width, the low-energy ions stay longer in the sheath and see a greater voltage spread, resulting in the disappearance of the low-energy peak. If $\tau_{ion}/\tau_{rf} \sim \gamma > 1$, the oscillating sheath boundary should cross the ion's path about γ times, resulting in γ intervals when the ion experiences zero electric field. However, for constant sheath width, the ion is continually accelerated once it enters the sheath, resulting in IEDs shifted toward higher energies. This is why in Tsui's IEDs the low-energy peaks become smaller as τ_{ion}/τ_{rf} enters the intermediate-frequency regime. This implies that sheath width oscillation must be included in order to obtain correct IEDs for all τ_{ion}/τ_{rf}, but constant sheath width is a valid assumption for the high-frequency regime.

4. Collisional effects and ion angular distribution

The ion angular distribution (IAD) in a plasma reactor is anisotropic at the presheath–sheath boundary and at the target surface. The electric field is normal to the target surface in both the presheath and sheath. So, when an ion traverses the presheath and sheath, only its velocity component normal to the target surface is accelerated. In a typical discharge, $T_e \gg T_i$. The Bohm criterion dictates that before an ion enters the sheath from the presheath, its velocity component normal to the target surface must be accelerated from an initial low thermal velocity in the bulk ($\approx (kT_i/M)^{1/2}$) to the Bohm velocity, $u_B = (kT_e/M)^{1/2}$. Since its velocity component parallel to the surface is not accelerated from the low thermal value, the ion is anisotropic at the presheath–sheath boundary. The anisotropy is enhanced at the target as the ion's velocity component normal to the target surface is further accelerated by the sheath electric field. This implies that faster higher energy ions hit the target with narrower impact angles than slower lower energy ions.

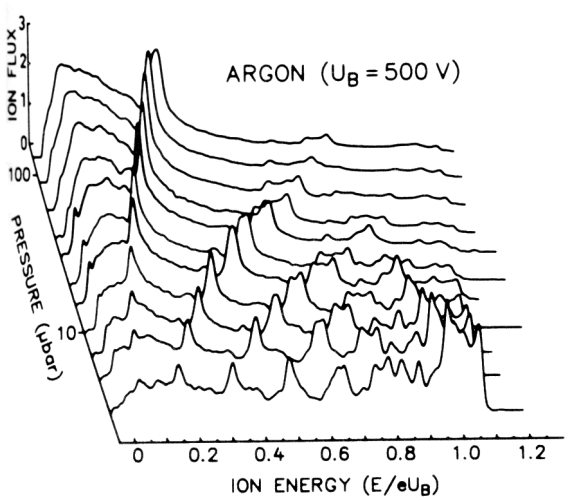

Figure 15. IEDs measured in a collisional rf argon discharge for various pressures from Wild and Koidl [6]. The secondary IED peaks arise from a combination of charge exchange collisions and rf modulation.

Let us measure the angle of incidence of an impinging ion relative to the target surface normal. For the high-frequency ($\tau_{ion}/\tau_{rf} \gg 1$) regime, the IED is narrow and centred about $e\bar{V}_s$, where $\bar{V}_s$ is the dc sheath voltage drop. Typically, $e\bar{V}_s \gg kT_i$. So, in the high-frequency regime, most of the ions hit the target with high energies and narrow impact angles, resulting in a narrow IAD. In contrast, for the low-frequency regime ($\tau_{ion}/\tau_{rf} \ll 1$), the IED is broad and bimodal with a dominant low-energy peak at the dc floating potential V_F (29) and a high-energy peak at the maximum target sheath voltage drop V_{Tmax}. Typically, $V_F \gg kT_i$, but $V_F \ll V_{Tmax}$. So, in the low-frequency regime, many ions hit the target with relatively lower energies and wider impact angles, resulting in a wider IAD. In other words, for $\tau_{ion}/\tau_{rf} \ll 1$, the IAD width is closely related to the low-energy component of the IED.

In collisionless sheaths, given the initial ion velocity distribution at the sheath edge, the IAD can be deduced from the IED. This is because both the velocity component normal to and parallel to the target surface contribute to the total ion impact energy, but only the velocity component normal to the target surface is accelerated by the electric field and differs from its initial value. Thus, given the final ion impact energy and the initial ion velocity, one can determine the final velocity components both normal to and parallel to the target surface. This, in turn determines the angle at which the ion hits the target surface.

However, for collisional sheaths, the above is no longer true since collisions can affect motion parallel to the target surface. Collisional effects become important in conventional RIE reactors operated at high pressure. Both elastic and charge exchange collisions occur in the sheath and affect the IED and IAD. In elastic collisions, fast ions scatter against slow thermal neutrals more or less isotropically. In charge exchange collisions, fast ions transfer their charge to slow thermal neutrals, resulting in fast neutrals and slow thermal ions.

Both types of collisions broaden the IED and shift it towards lower energies. Davis and Vanderslice [44] were among the first to present experimental measurements of IEDs in *dc* glow discharges. Their measurements were made at relatively high pressures where the sheaths were highly collisional, and most ions arrived at the target with low energies. They also presented a simple model to describe IEDs in a dc collisional sheath, which compared well with their empirical IEDs and which has been verified by other experiments and simulations (Vahedi *et al* [45]). They calculated the IED resulting from ion collisional drift across a time-averaged linear sheath electric field, assuming no ionizing collisions within the sheath. The resulting IEDs were broad, smooth and skewed toward lower energies.

In *rf* sheaths, charge exchange collisions can lead to the formation of secondary IED peaks which are at lower energies than the two primary IED peaks (see figure 15). The number of secondary peaks is roughly equal to the average number of rf periods it takes an ion to cross the sheath. Thus, secondary IED peaks are observable only for $\tau_{ion}/\tau_{rf} > 1$. The origin of these peaks was first described by Wild and Koidl [5]. Recall that the two primary peaks are due to the rf modulation of slow ions which entered the sheath at the sheath edge and did not experience collisions. Similarly, the secondary peaks are due to the rf modulation of the slow ions created by charge exchange collisions within the sheath. These peaks are at lower energies, because the slow ions that are formed inside the sheath do not experience the full potential drop of the ions entering at the sheath edge.

Suppose an ion is traversing an rf sheath with $\tau_{ion}/\tau_{rf} = \gamma$ with $\gamma > 1$, i.e. it takes an ion about γ rf periods to cross the sheath. As the ion traverses the sheath, the electron front $s_e(t)$ will be periodically sloshing back and forth from the target about γ times. Suppose we look at a position s_0 inside the sheath at a time t_0 when the electron front passes by s_0 on its way to the target. During the time interval it takes the electron front to reach the target, bounce back and pass by s_0 again, the local electric field at s_0 is zero. Thus any secondary ions created at s_0 during this time interval will be virtually at rest and accumulate at s_0. However, when the receding electron front passes by s_0 again, the electric field at s_0 reappears and accelerates the bunched ions towards the target. The bunched ions reach the target with the same impact energy E, causing a peak in the IED. In other words, for a fixed s_0, we get an IED peak, when $\mathrm{d}E/\mathrm{d}(\omega t_0) = 0$.

The above analysis, however, is missing one crucial point. Secondary ions can be created at every point s_0 within the sheath so that IED peaks generated by bunched ions created at different s_0 will wash each other out. Thus, not only must the secondary ions be created at phase angles ωt_0 such that $\mathrm{d}E/\mathrm{d}(\omega t_0) = 0$, but they must also be created at positions s_0 within the sheath such that $\mathrm{d}E/\mathrm{d}s_0 = 0$. This occurs only at discrete s_0, resulting in discrete secondary IED peaks. While an ion traverses the sheath, the electron front will be moving back and forth from the target about γ times. Thus, there are at most γ positions within the sheath where the electron front can intersect the ion's path, This explains qualitatively why the number of secondary IED peaks roughly equals $\gamma = \tau_{ion}/\tau_{rf}$.

Thus, collisional IEDs consist of both a broad continous time-averaged background skewed toward lower energies (described by Davis and Vanderslice), as well as structures

due to rf modulation and charge exchange collisions (described by Wild and Koidl). Also note from figure 15 that at higher pressures elastic scattering (which only contributes to the stationary background) begins to dominate over charge exchange collisions and washes out the IED peaks.

Elastic scattering can result in ions with appreciable velocity parallel to the target surface and can significantly broaden the IADs of ions hitting the target. Charge exchange collisions result in slow ions with no appreciable velocity parallel to the target surface. When the electric field accelerates these ions, most of their velocity will be normal to the target surface. However, the IAD is still broadened compared to the collisionless case, since charge exchange collisions decrease the ratio of the velocity component normal to the target surface over the velocity component parallel to the target surface. Because charge exchange collisions can produce fast neutrals that bombard the target, it may be necessary to consider neutral energy and angular distributions when calculating sputter and etch yields in collisional sheaths [8, 18].

5. Simulations of collisional rf discharges

In order to study collisional effects on the IEDs at the electrodes of rf discharges, several authors have used either Monte Carlo or PIC methods to follow the trajectory of particles in the presence of collisions.

5.1. Monte Carlo simulations

Both Kushner [15] and Barnes *et al* [17] used Monte Carlo simulations to study the IED of ions in low-pressure capacitively coupled rf discharges. Although both Kushner and Barnes *et al* included collisions in their models, collisional effects were not significant at the low pressures they considered. Kushner assumed a time-varying spatially linear sheath electric field given by $\mathcal{E}(x,t) = -2V_s(t)[s(t) - x]/s(t)^2$, where $V_s(t)$ is assumed to be a half-wave rectified sinusoid typical of low-frequency resistive sheaths and $s(t)$ is assumed to be sinusoidal. Barnes *et al* assumed a spatially nonlinear time-varying electric field given by Lieberman [39]. Both Kushner and Barnes *et al* saw the familiar bimodal collisionless IEDs and noted the dependence of the IED shapes on τ_{ion}/τ_{rf}.

5.2. PIC simulations

PIC simulations of rf discharges are attractive because the fields and energy distributions can be obtained self-consistently from first principles [46]. No assumptions need be made about the electric field or the bulk plasma velocity distributions. Also, collisional effects can be included in PIC models by coupling PIC methods with Monte Carlo collision (MCC) models [46]. The only disadvantage of PIC methods is that they tend to be computationally expensive compared to other numerical methods. However, with the growing availability of fast, affordable workstations, this is no longer a significant drawback, especially for one-dimensional (1D) simulations [47].

Vender and Boswell [19] simulated a 1D parallel plate rf hydrogen discharge. The neutral pressure was 20 mTorr, the electrode spacing was 20 cm and the discharge was driven by a sinusoidal voltage source of amplitude 1 kV and frequency 10 MHz. The ion transit time τ_{ion} across the sheath was roughly 3×10^{-7} s which corresponded to 3 rf cycles. The model included ionizing collisions but no elastic collisions. When charge exchange collisions were omitted, the PIC simulations yielded the familiar double-humped collisionless IEDs. The simulated IEDs were compared to the high-frequency regime IED (10) derived by Benoit-Cattin *et al* and found to be in good agreement. When charge exchange was taken into account, the PIC IEDs showed the secondary structures described by Wild and Koidl [5]. Vender and Boswell also noted that when the frequency was changed from 10 MHz ($\tau_{ion}/\tau_{rf} \sim 3$) to 1 MHz ($\tau_{ion}/\tau_{rf} \sim 0.3$), the sheath voltage changed from a sinusoid to a half-wave rectified signal, indicating a transition from a capacitive to a resistive sheath regime.

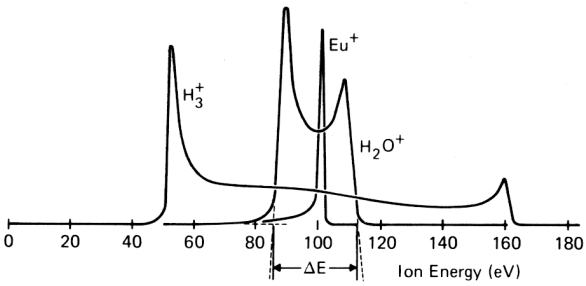

Figure 16. IEDs from Coburn and Kay [23] for H_3^+, H_2O^+ and Eu^+ ions at the grounded electrode of a 75 mTorr argon rf discharge driven at 13.56 MHz.

Surendra and Graves [20] conducted 1D PIC simulations of an rf parallel-plate collisional helium discharge. The model included elastic and ionizing electron–neutral collisions and charge exchange ion–neutral collisions but no elastic ion–neutral collisions. The neutral pressure was 250 mTorr, the electrode spacing was 4 cm and the frequency of the voltage source driving the discharge was either 12 MHz or 30 MHz. The applied rf voltage varied from 200 to 500 V for the 12 MHz case, while it varied from 50 to 200 V for the 30 MHz case. As expected, the simulated collisional IEDs were skewed toward lower energies. In the 30 MHz cases, the IEDs showed the secondary charge exchange peaks described by Wild and Koidl. In the 12 MHz cases, the IEDs did not appear to have multiple structures. This leads us to assume that $\tau_{ion}/\tau_{rf} \lesssim 1$ for the 12 MHz cases. Recall from section 4 that $\tau_{ion}/\tau_{rf} > 1$ is required to see an IED with multiple secondary peaks.

6. Experiments

One of the earliest works to show rf ion modulation was the laboratory measurements of Erö [21]. He experimentally measured the IED in a Thonemann ion source using an electrostatic analyser and observed the effect of rf modulation on IED width ΔE_i. His ion energy spectra had the characteristic bimodal shape, already shown in figure 1. He observed qualitatively that as the applied rf voltage was raised, ΔE_i increased.

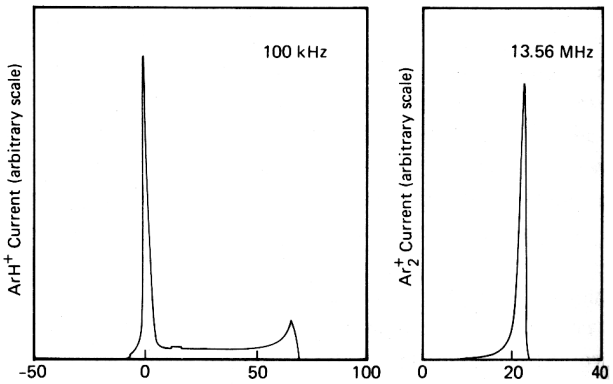

Figure 17. IEDs at the ground electrode of an rf argon discharge from Kohler *et al* [24]. Excitation frequencies were at 100 KHz and 13.56 MHz.

Coburn and Kay [23] presented experimental measurements of the IEDs of contaminant ion species (H_3^+, H_2O^+ and Eu^+) in a 75 mTorr capacitively coupled argon discharge driven at 13.56 MHz. The ion energies and ion masses were measured at the grounded electrode by an electrostatic deflection analyser and a quadrupole mass spectrometer, respectively. They observed bimodal IEDs with peak splitting decreasing with increasing ion mass M. In fact, for the heaviest ions (Eu^+), the observed IED was singly peaked at the dc sheath voltage. Thus, for larger values of τ_{ion}/τ_{rf} (e.g. larger M), the IEDs became narrower, as expected (see figure 16). Their results also show that for low τ_{ion}/τ_{rf} (e.g. small M), the low-energy peak of the IED dominates.

Kohler *et al* [24] measured the IEDs at the grounded electrode of a 50 mTorr capacitively coupled argon rf plasma reactor for frequencies of 70 kHz to 13.56 MHz. They also used an electrostatic deflection analyser in combination with a quadrupole mass spectrometer. The observed IEDs were narrower at higher frequencies (higher τ_{ion}/τ_{rf}) and the lower energy peak dominated at lower frequencies (lower τ_{ion}/τ_{rf}) (see figure 17).

The Kuypers and Hopman experiments [25, 26] were the first results of energy measurements with an electrostatic parallel-plate analyser at the powered rather than grounded electrode of an rf reactor. This was technically difficult because the potential of the analyser had to follow the rf signal. Kuypers and Hopman used optical fibres to transmit data to and from the analyser (i.e. to control the voltage applied between the plates of the analyser and to measure the bombarding ion current). Energy measurements were performed on asymmetric low-pressure (2–3 mTorr) argon, oxygen and CF_4 discharges driven at 13.56 MHz. For each ion species, there were two IED peaks centred at $e\bar{V}_s$ with a peak splitting decreasing with increasing ion mass (see figure 18). The measured energy spectrums agreed well with the high-frequency regime IEDs derived by Benoit-Cattin *et al* [9]. Although no mass spectrometer was used in the experiment, Kuypers and Hopman used the theoretical dependence of ΔE_i with M (11) derived by Benoit-Cattin and Bernard [10] to mass resolve their experimental IEDs. By fitting (11) with the empirical results, Kuypers and Hopman also determined the average sheath thickness $\bar{s}$. This $\bar{s}$ was plugged into the collisionless Child–Langmuir current law (38) to determine the theoretical ion current entering the extraction hole. This was compared to the actual measurements of total ion current through the extraction hole and found to be in good agreement. This confirmed that the sheath under study was well represented by a collisionless sheath.

Wild and Koidl [5, 6] measured IEDs at the grounded electrode of an asymmetric, capacitively coupled rf discharge under conditions such that charge exchange collisions dominated the sheath. Wild and Koidl inverted the electrode geometry so that the rf power source was connected to the larger electrode while the smaller electrode was grounded. Thus, they were able to measure ion energies at the smaller electrode (which has the larger ion bombarding energies)

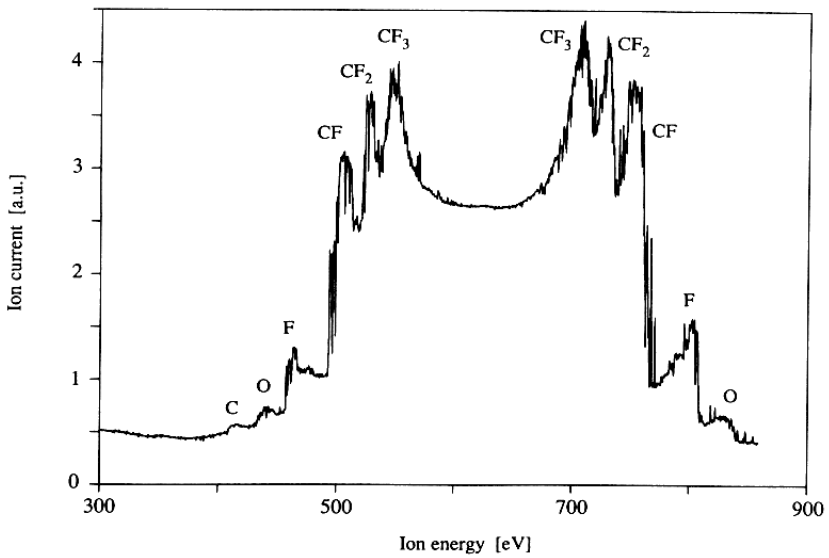

Figure 18. IEDs at the powered electrode of an rf CF_4 discharge driven at 13.56 MHz from Kuypers and Hopman [26].

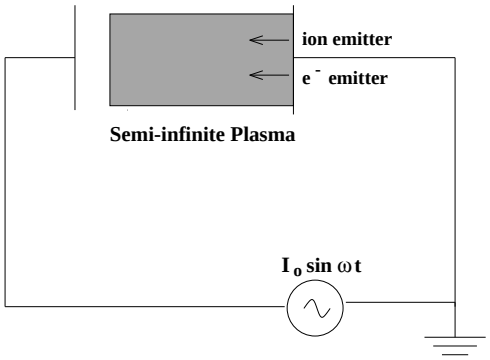

Figure 19. The PDP1 model of a current-driven sheath.

without having to use sophisticated optical techniques. The ion impact energies were measured by a retarding grid analyser located at the grounded electrode. Energy measurements were made on argon and oxygen discharges driven at 13.56 MHz at pressures in the range ∼2–100 mTorr. In addition to the two primary IED peaks due to ions which do not suffer collisions in the sheath, Wild and Koidl observed several secondary IED peaks which they attributed to a combination of charge exchange collisions and rf modulation. At the higher pressures, the IED peaks were washed out and the IED was broadened and shifted toward lower energies, probably due to the increasing dominance of elastic collisions (see figure 15). To explain the origin of the peaks Wild and Koidl presented a model (see section 4) for ion transport through an rf sheath which included the creation of slow secondary ions in the sheath via charge exchange and a parametric expression for the sheath electric field $\mathcal{E} \sim x^{\nu}$. They showed that the position of the secondary IED peaks depended on the spatial variation of the sheath electric field and a discharge scaling parameter $\eta = e\bar{V}_s/(M\omega^2 d^2) \sim (\tau_{rf}/\tau_{ion})^2$.

Manenschijn *et al* [27] used a similar apparatus to Kuypers and Hopman to take ion energy measurements at the powered electrode of a capacitively coupled rf parallel-plate reactor operating at 13.56 MHz, but for a wider range of pressures (2–300 mTorr) and a wider variety of gases (Ar, Ar/H_2, N_2, O_2, SF_6/He and Cl_2) discharges. For low pressures, they saw the typical collisionless bimodal IED for each ion species with the peak splitting $\sim M^{-1/2}$. For higher pressures, they also saw the secondary peaks due to charge exchange collisions described by Wild and Koidl [5]. At the highest pressures, they also observed the general broadening and washing out of the peaks that occur due to elastic scattering.

7. PIC simulation of a current-driven rf sheath

We conducted a variety of PIC simulations of a current-driven collisionless rf plasma sheath in order to obtain IEDs for a wide range of τ_{ion}/τ_{rf}. Figure 19 shows our model for the current-driven sheath. We used our bounded 1d3v PIC plasma code PDP1 [46, 48]. In the simulation, there were two symmetric planar electrodes connected by an external circuit. The source electrode was grounded and the target electrode was driven by a sinusoidal current source. Electrons

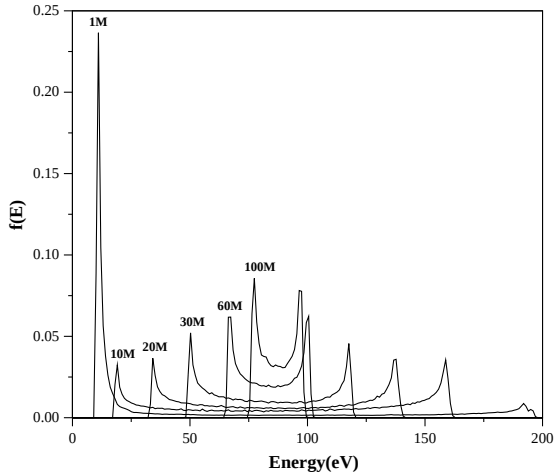

Figure 20. PDP1 results showing IEDs of helium ions hitting the target electrode of rf discharges driven at frequencies from 1 MHz to 100 MHz. The maximum sheath drop V_{Tmax} was about 200 V in every case.

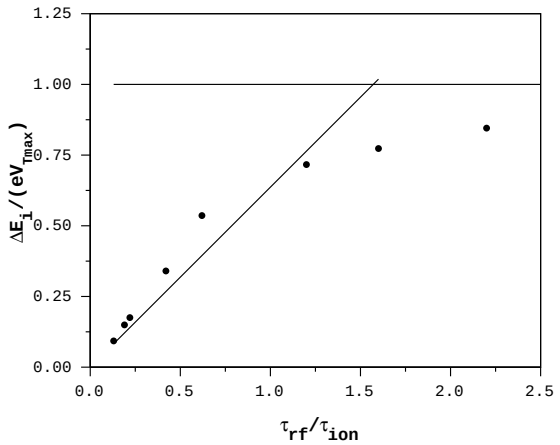

Figure 21. Normalized IED width versus τ_{rf}/τ_{ion} for the IED curves in figure 20.

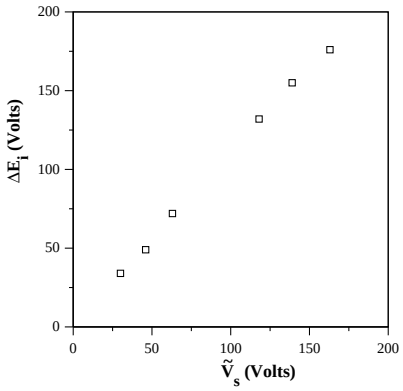

Figure 22. PDP1 results showing IED width versus $\tilde{V}_s$ for CF_3 ions in an rf discharge.

and helium ions were emitted from the source electrode at thermal velocities. As electrons and helium ions accumulated between the electrodes, an rf ion sheath developed at the target electrode. After a steady state was reached, various diagnostics were recorded. We chose a current-driven sheath in order to avoid arbitrarily setting the target potential dc bias.

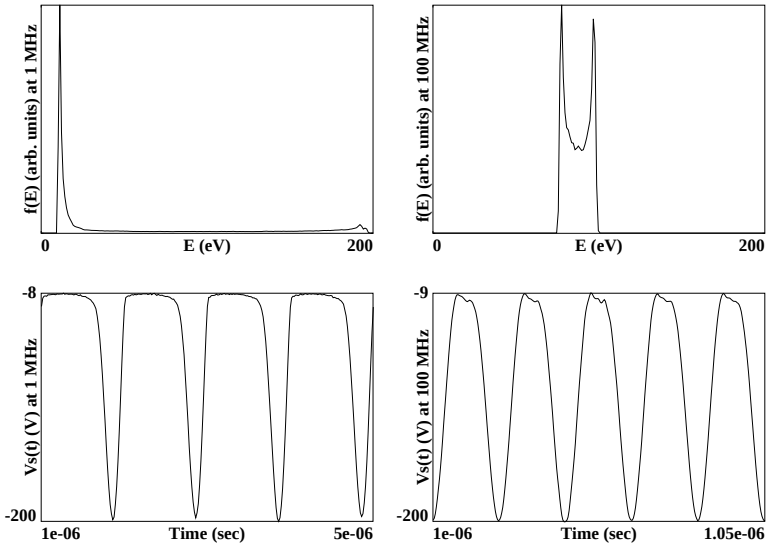

Figure 23. PDP1 results showing IEDs and sheath voltages $V_s(t)$ for helium rf discharges driven at 1 MHz and 100 MHz, respectively.

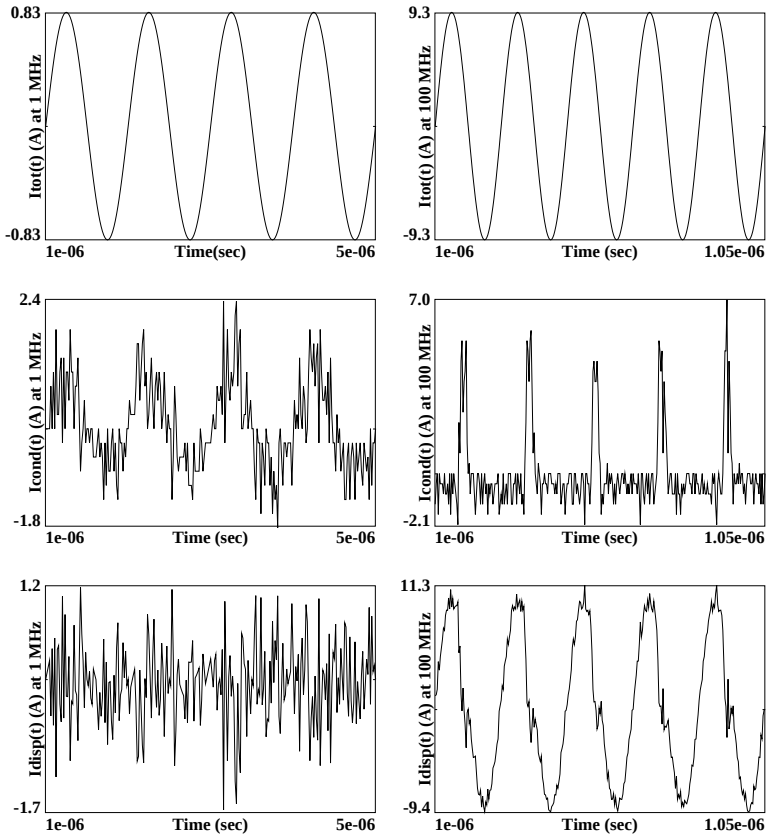

Figure 24. PDP1 results showing the total, conduction and displacement currents for helium rf discharges driven at 1 MHz and 100 MHz, respectively.

Figure 20 shows the IEDs for various applied frequencies. In each case, input parameters were chosen so that the ion transit frequency $\omega_{ion}/(2\pi) \approx 13$ MHz. As expected, we see bimodal distributions which become narrower as the frequency increases.

Figure 21 is a plot of $\Delta E_i/(eV_{Tmax})$ versus τ_{rf}/τ_{ion}, where V_{Tmax} is the maximum sheath voltage drop. The dots represent the simulation data while the two lines represent the low- and high-frequency limits for $\tau_{rf}/\tau_{ion} \ll 1$ and $\tau_{rf}/\tau_{ion} \gg 1$. Recall that for the high-frequency regime, ΔE_i should increase linearly with τ_{rf}/τ_{ion} (see (9)) and for the low-frequency regime, $\Delta E_i/e$ should approach the maximum sheath voltage drop. For our simulations, the maximum sheath voltage drop was about 200 V. The simulation appears to agree reasonably well with the theory.

From (9), we also know that for low τ_{rf}/τ_{ion}, ΔE_i is a linear function of $\tilde{V}_s$, the rf part of the sheath voltage. We conducted a complementary set of simulations in which τ_{rf}/τ_{ion} was held fixed while we varied $\tilde{V}_s$. Figure 22 shows the results of these simulations, showing the expected linear relation between ΔE_i and $\tilde{V}_s$. For this set of simulations, we used CF_3 rather than He ions and kept the frequency of the current source fixed at 13.56 MHz.

For low frequencies (i.e. $\tau_{ion}/\tau_{rf} \ll 1$), we expect the sheath voltage to stay at a minimum value for a longer part of the cycle than at a maximum value, resulting in an IED with a dominant low-energy peak, whereas for high frequencies (i.e. $\tau_{ion}/\tau_{rf} \gg 1$) we expect the sheath voltage to be nearly sinusoidal, resulting in peaks of more or less equal heights. From figure 23, we see that the sheath voltage waveforms and the relative dominance of the peaks are as expected. In the high-frequency regime (e.g. 100 MHz), the IED peaks are nearly equal in height and $V_s(t)$ resembles a sinusoidal wave. In the low-frequency case (e.g. 1 MHz), the low-energy peak of the IED dominates and $V_s(t)$ resembles a half-wave rectified signal.

Also, from figure 24, we see that for the low-frequency regime (e.g. 1 MHz) the conduction current dominates and the sheath is resistive, while for the high-frequency regime (i.e. 100 MHz) the displacement current dominates and the sheath is capacitive. The jagged shape of the waveforms is due to statistical noise.

8. Conclusion

For collisionless rf plasma sheaths, the ratio τ_{ion}/τ_{rf} determines the nature of the sheath, the sheath voltage waveform and the shape of the IEDs. For, $\tau_{ion}/\tau_{rf} \ll 1$, the sheath is resistive, the sheath voltage is a half-wave rectified signal and the IED is broad and bimodal with a dominant low-energy peak. As τ_{ion}/τ_{rf} is increased, the sheath becomes capacitive, the sheath voltage becomes sinusoidal, the two IED peaks become more equal in height and the peak splitting decreases until at some point the two peaks merge and cannot be resolved.

Acknowledgments

We are especially grateful to our major supporters AFOSR contract F49620-94-1-0387 and ONR contract N00014-97-1-0241. There has also been continued support from LLNL, plus collaborations in the plasma processing area, for the best part of a decade, for which we are very grateful. This work was also partially supported by National Science Foundation Grant ECS-9202993, a gift from the Lam Research Corporation and the University of California Semiconductor Manufacturing Alliance for Research and Training.

Appendix. Calculation of IED and ΔE_i for $\tau_{ion}/\tau_{rf} \gg 1$

We begin with the equation of motion under the assumption of a uniform sheath field and a sinusoidal sheath voltage

$$M\frac{dv}{dt} = \frac{e}{s}(\bar{V}_s + \tilde{V}_s \sin\omega t). \tag{58}$$

Let t_0 be the time an ion enters the sheath. Let t_f be the time the ion hits the target. Then, integrating the equation of motion once and assuming $v(t_0) = 0$, we obtain

$$Mv(t_f) = \frac{e\bar{V}_s}{s}(t_f - t_0) + \frac{e\tilde{V}_s}{\omega s}(\cos\omega t_f - \cos\omega t_0). \tag{59}$$

Let us define the dimensionless parameter

$$A_1 \equiv \frac{\omega^2 s(t)^2 M}{e\bar{V}_s}. \tag{60}$$

From the expression for τ_{ion}/τ_{rf} given in (3), we see that $A_1 = 8\pi^2/9(\tau_{ion}/\tau_{rf})^2$. Using $E = Mv(t_f)^2/2$ for the target energy and rearranging (59), we get an expression for the normalized energy,

$$\frac{E}{e\bar{V}_s} = \frac{1}{2A_1}\left[\omega(t_f - t_0) - \frac{\tilde{V}_s}{\bar{V}_s}(\cos\omega t_f - \cos\omega t_0)\right]^2. \tag{61}$$

When we now integrate (59), we obtain

$$\begin{aligned} s(t) = x(t_f) - x(t_0) &= \frac{e\bar{V}_s(t_f - t_0)^2}{2sM} \\ &+ \frac{e\tilde{V}_s(t_f - t_0)\cos\omega t_0}{\omega s M} \\ &- \frac{e\tilde{V}_s(\sin\omega t_f - \sin\omega t_0)}{s\omega^2 M}. \end{aligned} \tag{62}$$

Rearranging terms, we obtain an expression for A_1,

$$\begin{aligned} A_1 \equiv \frac{s^2 M\omega^2}{e\bar{V}_s} &= \frac{\omega^2(t_f - t_0)^2}{2} \\ &+ \frac{\tilde{V}_s}{\bar{V}_s}[\omega(t_f - t_0)\cos\omega t_0 - (\sin\omega t_f - \sin\omega t_0)]. \end{aligned} \tag{63}$$

Now, when we assume the high-frequency case, then the ion transit time across the sheath is much larger than the rf period. This implies that $\omega(t_f - t_0) \gg 1$. It also implies that $A_1 \sim (\tau_{ion}/\tau_{rf})^2 \gg 1$. So, using (61) for the normalized energy and (63) for A_1, we note that the terms proportional to $\omega(t_f - t_0)$ or $\omega^2(t_f - t_0)^2$ are much larger than the other terms which are roughly of order unity. Thus, we can write

$$\frac{E}{e\bar{V}_s} \approx \frac{1}{A_1}\left[\frac{\omega^2(t_f - t_0)^2}{2} - \frac{\tilde{V}_s}{\bar{V}_s}\omega(t_f - t_0)(\cos\omega t_f - \cos\omega t_0)\right] \tag{64}$$

and

$$A_1 \approx \frac{\omega^2(t_f - t_0)^2}{2} + \frac{\tilde{V}_s}{\bar{V}_s}\omega(t_f - t_0)\cos\omega t_0. \tag{65}$$

Then, we find

$$\begin{aligned} \frac{E}{e\bar{V}_s} &\approx \frac{1}{A_1}\left[A_1 - \frac{\tilde{V}_s}{\bar{V}_s}\omega(t_f - t_0)\cos\omega t_f\right] \\ &= 1 - \frac{\tilde{V}_s}{\bar{V}_s A_1}\omega(t_f - t_0)\cos\omega t_f. \end{aligned} \tag{66}$$

Also, solving for $\omega(t_f - t_0)$ in the expression for A_1 (65), we obtain

$$\omega(t_f - t_0) = \sqrt{2A_1} + \Theta(1). \tag{67}$$

Note that because $A_1 \gg 1$, the $\Theta(1)$ expression may be neglected. Substituting (67) into (66) for normalized energy, we obtain

$$\frac{E}{e\bar{V}_s} \approx 1 - \sqrt{\frac{2}{A_1}}\frac{\tilde{V}_s}{\bar{V}_s}\cos\omega t_f. \tag{68}$$

This implies that the normalized energy spread is

$$\frac{\Delta E_i}{e\bar{V}_s} = 2\sqrt{\frac{2}{A_1}}\frac{\tilde{V}_s}{\bar{V}_s} = \frac{2\tilde{V}_s}{\bar{V}_s\omega s}\left(\frac{2e\bar{V}_s}{M}\right)^{1/2}. \tag{69}$$

This is equivalent to Benoit-Cattin *et al*'s expression for ΔE_i (9). To obtain the ion energy distribution, we note that

$$f(E) = \frac{\mathrm{d}n}{\mathrm{d}E} = \frac{\mathrm{d}n}{\mathrm{d}t_0}\frac{\mathrm{d}t_0}{\mathrm{d}E}. \tag{70}$$

If we assume constant ion flux, then $\mathrm{d}n/\mathrm{d}t_0 \equiv n_t$ is a constant. Substituting (67) and (69) into (68), we obtain

$$E - e\bar{V}_s \approx \frac{\Delta E_i}{2}\cos(\omega t_0 + \sqrt{2A_1}). \tag{71}$$

This implies that

$$\frac{\mathrm{d}E}{\mathrm{d}t_0} \approx \frac{\Delta E_i}{2}\omega\sin(\omega t_0 + \sqrt{2A_1}). \tag{72}$$

Substituting this into (70) for $f(E)$ and using the trigonometric identity $\sin\theta = \sqrt{1-\cos^2\theta}$, we obtain Benoit-Cattin *et al*'s expression

$$f(E) = \frac{\mathrm{d}n}{\mathrm{d}E} = \frac{2n_t}{\Delta E_i\omega}\left[1 - \frac{4}{\Delta E_i^2}(E - e\bar{V}_s)^2\right]^{-1/2}. \tag{73}$$

Benoit-Cattin *et al* also made the additional assumption that $\tilde{V}_s/\bar{V}_s \ll 1$. However, from the above derivation, we see that this assumption is not necessary to derive equations (9) and (10), provided that we assume that the ion transit time is much larger than the rf period.

References

[1] Charles C, Boswell R W and Porteous R K 1992 Measurement and modeling of ion energy distribution functions in a low pressure argon plasma diffusing from a 13.56 MHz helicon source *J. Vac. Sci. Technol.* A **10** 398

[2] Gottscho R A 1993 Ion transport anisotropy in low pressure, high-density plasmas *J. Vac. Sci. Technol.* B **11** 1884

[3] Holber W M and Forster J 1990 Ion energetics in electron cyclotron resonance discharges *J. Vac. Sci. Technol.* A **8** 3720

[4] Hopwood J 1993 Ion bombardment energy distributions in a radio frequency induction plasma *Appl. Phys. Lett.* **62** 940

[5] Wild C and Koidl P 1989 Structured ion energy distribution in radio frequency glow-discharge systems *Appl. Phys. Lett.* **54** 505

[6] Wild C and Koidl P 1990 Ion and electron dynamics in the sheath of radio-frequency glow discharges *J. Appl. Phys.* **69** 2909

[7] Liu J, Huppert G L and Sawin H H 1990 Ion bombardment in rf plasmas *J. Appl. Phys.* **68** 3916

[8] Manenschijn A and Goedheer W J 1991 Angular ion and neutral energy distribution in a collisional rf sheath *J. Appl. Phys.* **69** 2923

[9] Benoit-Cattin P, Bernard L C and Bordenave-Montesquieu A 1967 Dispersion en énergie des ions produits par une source à excitation de haute fréquence *Entropie* **18** 29

[10] Benoit-Cattin P and Bernard L C 1968 Anomalies of the energy of positive ions extracted from high-frequency ion sources. A theoretical study *J. Appl. Phys.* **39** 5723

[11] Farouki R T, Hamaguchi S and Dalvie M 1992 Analysis of a kinematic model for ion transport in rf plasma sheaths *Phys. Rev.* A **45** 5913

[12] Tsui R T C 1968 Calculation of ion bombarding energy and its distribution in rf sputtering *Phys. Rev.* **168** 107

[13] Metze A, Ernie D W and Oskam H J 1989 The energy distribution of ions bombarding electrode surfaces in rf plasma reactors *J. Appl. Phys.* **65** 993

[14] Field D, Klemperer D F, May P W and Song Y P 1991 Ion energy distributions in radio-frequency discharges *J. Appl. Phys.* **70** 82

[15] Kushner M J 1985 Distribution of ion energies incident on electrodes in capacitively coupled rf discharges *J. Appl. Phys.* **58** 4024

[16] Thompson B E, Sawin H H and Fischer D 1988 Monte-Carlo simulation of ion transport through rf glow-discharge sheaths *J. Appl. Phys.* **63** 2241

[17] Barnes M S, Forster J C and Keller J H 1991 Ion kinetics in low-pressure, electropoositive, RF glow discharge sheaths *IEEE Trans. Plasma Sci.* **19** 240

[18] May P W, Field D and Klemperer D F 1992 Modeling radio-frequency discharges: effects of collisions upon ion and neutral particle energy distributions *J. Appl. Phys.* **71** 3721

[19] Vender D and Boswell R W 1990 Numerical modeling of low-pressure RF plasmas *IEEE Trans. Plasma Sci.* **18** 725

[20] Surendra M and Graves D B 1991 Particle simulation of radio-frequency glow discharges *IEEE Trans. Plasma Sci.* **19** 144

[21] Erö J 1958 Radiofrequency modulation in the Thonemann ion source *Nucl. Instrum.* **3** 303

[22] Okamoto Y and Tamagawa H 1970 Energy dispersion of positive ions effused from an RF plasma *J. Phys. Soc. Japan* **29** 187

[23] Coburn J W and Kay E 1972 Positive-ion bombardment of substrates in rf diode glow discharge sputtering *J. Appl. Phys.* **43** 4965

[24] Kohler K, Horne D E and Coburn J W 1985 Frequency dependence of ion bombardment of grounded surfaces in rf argon glow discharges in a planar system *J. Appl. Phys.* **58** 3350

[25] Kuypers A D and Hopman H J 1988 Ion energy measurement at the powered electrode in an rf discharge *J. Appl. Phys.* **63** 1894

[26] Kuypers A D and Hopman H J 1990 Measurement of ion energy distributions at the powered rf electrode in a variable magnetic field *J. Appl. Phys.* **67** 1229

[27] Manenschijn A, Janssen G C A M, van der Drift E and Radelaar S 1991 Measurement of ion impact energy and ion flux at the rf electrode of a parallel plate reactive ion etcher *J. Appl. Phys.* **69** 1253

[28] Greene W M, Hartney M A, Oldham W G and Hess D W 1988 Ion transit through capacitively coupled Ar sheaths: Ion current and energy distribution *J. Appl. Phys.* **63** 1367

[29] Janes J and Huth C 1992 Energy-resolved angular distributions of O^+ ions at the radio-frequency-powered electrode in reactive ion etching *J. Vac. Sci. Technol.* A **10** 3086

[30] Janes J and Huth C 1992 Energy-resolved angular distributions of O^+ ions at the radio-frequency-powered electrode in reactive ion etching *J. Vac. Sci. Technol.* A **10** 3522

[31] Janes J 1993 Mass-selected ion angular impact energy distributions at the powered electrode in CF_4 reactive-ion etching *J. Appl. Phys.* **74** 659
[32] Olthoff J K, Van Brunt R J and Radovanov S B 1992 Ion kinetic-energy distributions in argon rf glow discharges *J. Appl. Phys.* **72** 4566
[33] Olthoff J K, Van Brunt J, Radovanov S B, Rees J A and Surowiec R 1994 Kinetic-energy distributions of ions sampled from argon plasmas in a parallel-plate, radio-frequency reference cell *J. Appl. Phys.* **75** 115
[34] Snijkers R J M M, van Sambeek M J M, Kroesen B M W and de Hoog F J 1993 Mass-resolved ion energy measurements at the grounded electrode of an argon rf plasma *Appl. Phys. Lett.* **63** 308
[35] Flender U and Wiesemann K 1994 Ion distribution functions behind an RF sheath *J. Phys. D: Appl. Phys.* **27** 509
[36] Metze A, Ernie D W and Oskam H J 1986 Application of the physics of plasma sheaths to the modeling of rf plasma reactors *J. Appl. Phys.* **60** 3081
[37] Song Y P, Field D and Klemperer D F 1990 Electrical potentials in RF discharges *J. Phys. D: Appl. Phys.* **23** 673
[38] Lieberman M A and Lichtenberg A J 1994 *Principles of Plasma Discharges and Material Processing* (New York: John Wiley)
[39] Lieberman M A 1988 Analytical solution for capacitive RF sheath *IEEE Trans. Plasma Sci.* **16** 4375
[40] Koenig H R and Maissel L I 1970 Application of RF discharges to sputtering *IBM J. Res. Dev.* **14** 168
[41] Riley M E 1995 Unified model of the RF plasma sheath *Sandia National Laboratories Technical Report* SAND95-0775 UC-401
[42] Riley M E 1996 Unified model of the RF plasma sheath II *Sandia National Laboratories Technical Report* SAND96-1948 UC-401
[43] Miller P A and Riley M E 1997 Dynamics of collisionless rf plasma sheaths *J. Appl. Phys.* **82** 3689
[44] Davis W D and Vanderslice T A 1963 Ion energies at the cathode of a glow discharge *Phys. Rev.* **131** 219
[45] Vahedi V, Lieberman M A, Alves M V, Verboncoeur J P and Birdsall C K 1991 A one-dimensional collisional model for plasma-immersion ion implantation *J. Appl. Phys.* **69** 2008
[46] Birdsall C K 1991 Particle-in-cell charged-particle simulations, plus Monte Carlo collisions with neutral atoms, PIC-MCC *IEEE Trans. Plasma Sci.* **19** 65
[47] Birdsall C K, Kawamura E and Vahedi V 1997 Progress in speeding up PIC-MCC codes applied to RF discharges *Int. Symp. on Plasma and Flow Simulation for Materials Processing (ISPFS) (Institute of Fluid Science, Tohoku University, Sendai, Japan, 1997)*
[48] PDP1 and other particle-in-cell codes may be downloaded from our web site at `http://ptsg.eecs.berkeley.edu`
[49] Llewelyn 1943 *Electron Inertia Effects* (Cambridge: Cambridge University Press)
[50] Birdsall and Bridges 1966 *Electron Dynamics of Diode Regions* (New York: Academic) ch 2